

PRECIOUS METALS IN SDSS QUASAR SPECTRA I: TRACKING THE EVOLUTION OF STRONG, $1.5 < Z < 4.5$ C IV ABSORBERS WITH THOUSANDS OF SYSTEMS

KATHY L. COOKSEY^{1,6}, MELODIE M. KAO², ROBERT A. SIMCOE³, JOHN M. O'MEARA⁴, AND J. XAVIER PROCHASKA⁵

Draft 4: November 2, 2021

ABSTRACT

We have vastly increased the C IV statistics at intermediate redshift by surveying the thousands of quasars in the Sloan Digital Sky Survey Data-Release 7. We visually verified over 16,000 C IV systems with $1.46 < z < 4.55$ —a sample size that renders Poisson error negligible. Detailed Monte Carlo simulations show we are approximately 50% complete down to rest equivalent widths $W_r \approx 0.6 \text{ \AA}$. We analyzed the sample as a whole and in ten small redshift bins with approximately 1500 doublets each. The equivalent width frequency distributions $f(W_r)$ were well modeled by an exponential, with little evolution in shape. In contrast with previous studies that modeled the frequency distribution as a single power law, the fitted exponential gives a finite mass density for the C IV ions. The co-moving line density dN_{CIV}/dX evolved smoothly with redshift, increasing by a factor of 2.37 ± 0.09 from $z = 4.55$ to 1.96, then plateauing at $dN_{\text{CIV}}/dX \approx 0.34$ for $z = 1.96$ to 1.46. Comparing our SDSS sample with $z < 1$ (ultraviolet) and $z > 5$ (infrared) surveys, we see an approximately 10-fold increase in dN_{CIV}/dX over $z \approx 6 \rightarrow 0$, for $W_r \geq 0.6 \text{ \AA}$. This suggests a monotonic and significant increase in the enrichment of gas outside galaxies over the 12 Gyr lifetime of the universe.

Subject headings: galaxies: halos – intergalactic medium – quasars: absorption lines – techniques: spectroscopic

Online-only material: color figures, machine-readable tables

1. INTRODUCTION

The study of the large-scale structure of the universe provides top-level constraints on models of galaxy evolution. Heavy elements are produced in the stars of galaxies. A variety of feedback processes move these metals from the sites of production into the intergalactic medium (IGM), enriching the material for future generations of stars. The cosmic enrichment cycle generically refers to the movement of gas from inside galaxies to the IGM and, possibly, back again (perhaps many times). The amount of heavy elements, the number of ionizing photons from galaxies and quasars, and the spatial distribution of material are driven by hierarchical structure formation and galactic processes such as star formation and feedback. Spectroscopic surveys of quasars yield a random sample of intervening absorbing gas clouds that can be used to constrain the on-going and summative enrichment processes in the universe.

C IV $\lambda\lambda 1548, 1550$ doublets are important tracers of the IGM and its evolution from $z \approx 6$ to today (Steidel 1990; Barlow & Tytler 1998; Ellison et al. 2000; Songaila 2001; Boksenberg et al. 2003; Schaye et al. 2003; Scannapieco et al. 2006; Danforth & Shull 2008; Ryan-Weber

et al. 2009; Becker et al. 2009; Cooksey et al. 2010; D'Odorico et al. 2010; Simcoe et al. 2011). This transition has been well-studied at $1.5 \lesssim z \lesssim 5.5$ for the following reasons. First, it is a strong transition of a common metal. Second, it is observable outside the Ly α forest, where it becomes easier to identify. Third, it redshifts into optical passbands at $z = 1.5$. Lastly, it is a resonant doublet, which gives it distinctive characteristics that enable surveys to be largely automated.

Observations of C IV doublets constrain the cumulative effect of the cosmic enrichment cycle. More specifically, the number and strength of C IV absorbers are affected by: the amount of carbon produced by all previous generations of stars; the spatial distribution of the element, driven by feedback processes; and the total ionizing radiation available to maintain the triply-ionized transition.

The intermediate-redshift C IV studies have traditionally found that the doublets follow a power law in the column density distribution function, with a slope of $\alpha \approx -1.8$, throughout the redshift range (Songaila 2001; Boksenberg et al. 2003; Scannapieco et al. 2006; D'Odorico et al. 2010). The earlier studies also measured a roughly constant C IV mass density for $2 < z < 4.5$ and $12 \lesssim \log N_{\text{CIV}} \lesssim 15$ absorbers (Songaila 2001; Boksenberg et al. 2003; Songaila 2005). Improved observations, pushing to bluer wavelengths (and hence lower redshift), have shown that Ω_{CIV} , the C IV mass density relative to the critical density, actually increases smoothly from $z = 4 \rightarrow 1.5$ (D'Odorico et al. 2010) and maps well onto the, $z < 1$ values, measured with *Hubble Space Telescope* (*HST*) ultraviolet spectra (Cooksey et al. 2010). Thus, Ω_{CIV} increases by, approximately, a factor of four over $z \approx 3 \rightarrow 0$ while dN_{CIV}/dX , the co-moving C IV line density, increases by a factor of two, roughly.

¹ MIT Kavli Institute for Astrophysics & Space Research, 77 Massachusetts Avenue, 37-685, Cambridge, MA 02139, USA; kcooksey@space.mit.edu

² Caltech, MC 249-17, 1200 East California Boulevard, Pasadena, CA 91125; mkao@caltech.edu

³ Department of Physics, MIT, 77 Massachusetts Avenue, 37-664D, Cambridge, MA 02139, USA; simcoe@space.mit.edu

⁴ Department of Chemistry and Physics, Saint Michael's College, One Winooski Park, Colchester, VT 05439; jomeara@smcvt.edu

⁵ Department of Astronomy & UCO/Lick Observatory, University of California, 1156 High Street, Santa Cruz, CA 95064, USA; xavier@ucolick.org

⁶ NSF Astronomy & Astrophysics Postdoctoral Fellow

Early infrared spectroscopy, which probes the $z \gtrsim 5$ universe, first resulted in a continuation of the roughly constant Ω_{CIV} out to $z \approx 6$ (Ryan-Weber et al. 2006; Simcoe 2006). However, with limited sightlines, these studies were highly susceptible to cosmic variance, as shown by later IR surveys, which reported that Ω_{CIV} actually dropped at $z \approx 6$ (Ryan-Weber et al. 2009; Becker et al. 2009). The latest and largest IR survey showed that Ω_{CIV} drops by, approximately, a factor of four over $z \approx 4 \rightarrow 6$ (Simcoe et al. 2011), and high-redshift quasars are continuing to be observed with the new Folded-port InfraRed EchelleTe (FIRE) on the Magellan/Baade Telescope (Simcoe et al. 2010). In addition, Simcoe et al. (2011) found that all previous high-redshift measurements overestimated Ω_{CIV} by $\approx 30\%$, since their lower-resolution IR spectra led to the lower-redshift Mg II $\lambda\lambda 2796, 2803$ being mis-identified as a strong, high-redshift C IV system.

The recent low (UV) and high (IR) redshift publications (Cooksey et al. 2010; Simcoe et al. 2011) have led us to assess the state of the intermediate (optical) redshift field (e.g., Songaila 2001; Boksenberg et al. 2003; Scannapieco et al. 2006; D’Odorico et al. 2010). The various studies have disparities in their definition of an absorber, completeness corrections, sensitivity limits, and/or adopted cosmology. Ideally, there should be a large, uniformly constructed, $0 < z < 6$ sample in order to evaluate the evolution of the C IV absorbers. We aim to produce an intermediate redshift catalog that is fairly comparable to the recent $z < 1$ and $z > 5$ catalogs.

For our $1.5 \lesssim z \lesssim 4.5$ survey, we use more than 26,000 quasar spectra in the Sloan Digital Sky Survey (SDSS; York et al. 2000) Data-Release 7 (DR7) database (Abazajian et al. 2009; Schneider et al. 2010), thus making this study the largest C IV survey—both in path length and in number of absorbers—to date. Others have mined SDSS quasar spectra for H I (e.g., Prochaska et al. 2005; Pieri et al. 2010b), Mg II (e.g., Nestor et al. 2005; Prochter et al. 2006), Ca II $\lambda\lambda 3934, 3969$ (e.g., Wild et al. 2006; Cherinka & Schulte-Ladbeck 2011), and O VI $\lambda, \lambda 1031, 1037$ (e.g., Frank et al. 2010; Pieri et al. 2010a). However, this is the first time that anyone has systematically searched for C IV, likely because it is more difficult and labor intensive, due to the increased amount of blending. This is the first in a series of papers on metals in SDSS quasar spectra, where we will assemble and analyze self-consistent catalogs of Si IV $\lambda\lambda 1393, 1402$, Mg II, and Ca II absorbers. These species are commonly studied in quasar absorption-line spectroscopy and typically trace the gas closest to galaxies.

We explain how we construct our C IV sample in §2 and our completeness corrections in §3. The main results are detailed in §4, and the discussion and summary are in §§5–6. We adopt the WMAP5 cosmology: $H_0 = 71.9 \text{ km s}^{-1} \text{ Mpc}$, $\Omega_{\text{M}} = 0.258$, and $\Omega_{\Lambda} = 0.742$ (Komatsu et al. 2009).

2. CONSTRUCTING THE C IV SAMPLE

2.1. SDSS Data-Release 7 Quasars

We began our survey with the 105,783 sightlines in the SDSS DR7 QSO catalog Schneider et al. (2010, also see Richards et al. 2002 for the SDSS quasar selection). SDSS spectra have wavelength coverage $3820 \text{ \AA} \leq \lambda \leq$

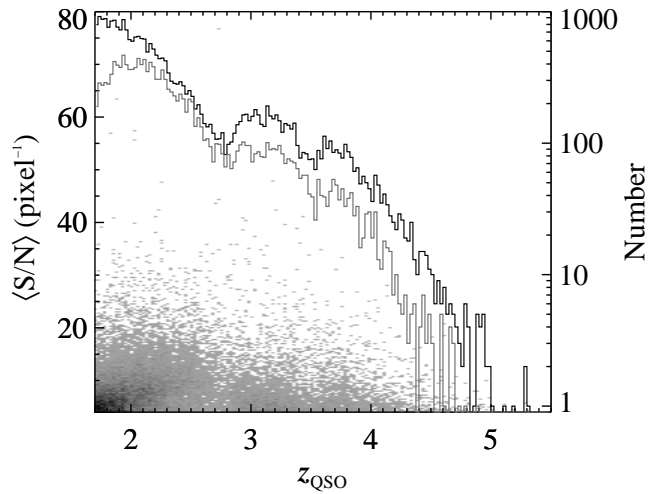


Figure 1. Redshift and $\langle \text{S/N} \rangle$ distribution of sightlines. Using the left-hand axis, the 2D histogram shows the median signal-to-noise and z_{QSO} space of the analyzed 26,030 spectra. The black and gray histograms give the redshift distribution for all spectra and for the 10,861 with confirmed C IV absorbers, respectively (right-hand axis).

9200 \AA and resolution varying from $R = 1850$ to 2200 (or 162 km s^{-1} to 136 km s^{-1}), and the reduced spectra are binned to a log-linear scale of $69 \text{ km s}^{-1} \text{ pixel}^{-1}$. We immediately excluded the 6,214 broad-absorption line (BAL) QSOs detailed in Shen et al. (2011).

We limited the sightlines to those with $z_{\text{QSO}} \geq 1.7$ and median signal-to-noise $\langle \text{S/N} \rangle \geq 4 \text{ pixel}^{-1}$ in the wavelength range sensitive to C IV absorbers (see Figure 1). This range depended on the quasar redshift and the SDSS wavelength coverage.

Previous, smaller surveys for C IV doublets have searched from the Ly α $\lambda 1215$ to C IV emission wavelengths. However, we removed a portion of this path length close to the Ly α emission to avoid possible confusion between the C IV doublet and any O I $\lambda 1302$, Si II $\lambda 1304$ pair. These latter two have a wavelength separation similar enough to the C IV doublet that automated search algorithms naturally bring in a large fraction of false positives. Since we had so much available path length available, we simply excluded a comfortable region around the O I, Si II “forest” in addition to the Ly α forest (i.e., $\lambda_r \geq 1310 \text{ \AA}$ in the restframe of the quasar). To exclude absorbers intrinsic to the QSO or affected by local ionization, clustering, and/or enrichment, we set the upper wavelength bound to $1548 \text{ \AA} (1 + z_{\text{QSO}}) (1 + \delta v_{\text{QSO}}/c)$,¹³ where we initially used $\delta v_{\text{QSO}} = -3000 \text{ km s}^{-1}$, but for the main analyses, the limit is $\delta v_{\text{QSO}} = -5000 \text{ km s}^{-1}$.

After the redshift, $\langle \text{S/N} \rangle$, and coverage cuts, we had 26,168 sightlines to search (see Table 1). Later, we excluded 138 sightlines as “visual BAL” QSOs for a final count of 26,030 spectra to analyze.

2.2. Automated Continuum Fitting

We generated individual quasar continua for all $\approx 26,000$ spectra in the sample using an algorithm which

¹³ Velocity offsets are defined as $\delta v = c(z - z_{\text{ref}})/(1 + z_{\text{ref}})$.

Table 1
Sightline Selection

Number	Description
105783	SDSS DR7 QSO catalog (Schneider et al. 2010)
99569	Excluding 6214 objects in BAL QSO catalog (Shen et al. 2011)
48260	Covering $\max[1310 \text{ \AA}(1 + z_{\text{QSO}}), 3820 \text{ \AA}] \leq \lambda < \min[1548 \text{ \AA}(1 + z_{\text{QSO}})(1 + \delta v_{\text{QSO}}/c), 9200 \text{ \AA}]^a$
26168	With $z_{\text{QSO}} \geq 1.7$ and $\langle S/N \rangle \geq 4 \text{ pixel}^{-1}$ in above wavelength range ^b
26030	Excluding 138 visual BAL QSOs
10861	With confirmed C IV doublets

^a The 1310 Å limit excludes the contaminating region in the O I, Si II “forest.” The fiducial value for $\delta v_{\text{QSO}} = -3000 \text{ km s}^{-1}$.

^b The details of these specific sightlines are given in Table 2.

Table 2
Sightline Summary

(1) QSO ID	(2) R.A.	(3) Decl.	(4) z_{QSO}	(5) $\langle S/N \rangle$ (pixel^{-1})	(6) f_{BAL}	(7) ΔX_{max}	(8) $\mathcal{N}_{\text{cand}}$	(9) \mathcal{N}_{CIV}	(10) $\delta X_{\text{C,IV}}$
52235-0750-082	00:00:09.38	+13:56:18.4	2.2342	5.94	0	1.33	0	0	...
52143-0650-199	00:00:09.42	-10:27:51.9	1.8449	4.68	0	0.83	1	1	0.028
52203-0685-198	00:00:14.82	-01:10:30.7	1.8877	5.16	0	1.24	0	0	...
52203-0685-439	00:00:15.47	+00:52:46.8	1.8516	8.64	0	2.16	0	0	...
54389-2822-315	00:00:24.83	+24:57:03.3	3.2137	9.21	0	1.48	0	0	...
51791-0387-167	00:00:39.00	-00:18:03.9	2.1249	6.61	0	1.75	0	0	...
52143-0650-178	00:00:50.60	-10:21:55.9	2.6404	8.68	0	1.56	4	2	0.083
52203-0685-154	00:00:53.17	-00:17:32.9	2.7571	7.55	0	1.15	0	0	...
52902-1091-546	00:00:57.58	+01:06:58.6	2.5551	11.83	0	1.78	3	2	0.084
51791-0387-093	00:00:58.22	-00:46:46.5	1.8973	13.27	0	0.84	1	1	0.037
52203-0685-134	00:01:25.14	+00:00:09.4	1.9739	5.32	0	1.52	0	0	...

Note. — Column 1 is the adopted QSO identifier from the spectroscopic modified Julian date, plate, and fiber number. Columns 2 through 4 are from the DR7 QSO catalog (Schneider et al. 2010). Column 5 is the median S/N measured in the region searched for CIV. The binary BAL flag f_{BAL} in Column 6 indicates which sightlines were considered BALs by at least one author (4) and which were confirmed by the authors as BALs to exclude (8). Column 7 is the maximum co-moving pathlength available in the sightline. Columns 8 and 9 give the number of candidate and confirmed CIV doublets, respectively. Column 10 is the pathlength blocked by the \mathcal{N}_{CIV} doublets in the sightline. (This table is available in a machine-readable form in the online journal. A portion is shown here for guidance regarding its form and content.)

combined principle-component analysis (PCA) fits, low-frequency b-spline correction, and automated outlier pixel and absorption-line exclusion. Since we are interested in C IV lines only, we limited the fit to $\lambda_r \geq 1230 \text{ \AA}$, redward of the Ly α forest. We discuss details of the method below so interested users may replicate it; the codes are also publicly available in the XIDL software library.¹⁴ Figure 2 shows example fits for eight spectra of varying $\langle S/N \rangle$ level.

First, every spectrum was iteratively fit using a 50-vector basis set of PCA “eigenspectra” from the SDSS DR1 quasar sample (Yip et al. 2004). The fit coefficients and their errors were determined using the algorithms of Connolly & Szalay (1999, Equations 4–6), with spectral pixels weighted by their inverse variance when quantifying the goodness-of-fit. The formal per-pixel error of the PCA continuum fit was negligible compared to the spectral shot noise.

A pixel exclusion mask was then generated upon each successive fit iteration. The initial mask consisted of the lowest 30% of pixels in successive 50-pixel windows, to filter strong absorption features and avoid biasing the continuum low on the critical initial fit. Then, for each subsequent iteration, a fresh mask was constructed which excluded pixels falling either less than -2σ or more than

3σ from the working continuum. This mask was further modified to include the neighboring pixels of each deviant pixel below the working continuum and exclude regions with three consecutive pixels above. The latter correspond to systematically errant regions of the fit that should actually be included, so they were unmasked automatically. This cycle was repeated with successive PCA fits until: (a) the mask converged so successive fits did not change; (b) the unmasked flux and continuum fit had median difference less than 0.001%; or (c) ten iterations passed.

For high-S/N spectra, low-frequency residuals in the PCA-normalized spectra become noticeable and affect our ability to search for weak C IV lines in the best data. We therefore performed a secondary correction to spectra with $\langle S/N \rangle \geq 8 \text{ pixel}^{-1}$, re-fitting the PCA-normalized spectrum with an additional third-order b-spline, with breakpoint spacing of 25 pixels (or 1725 km s^{-1}). As before, we used inverse-variance weighting and clipped outliers using the same thresholds. We refer below to this PCA plus b-spline fit as the “hybrid-continuum.”

The b-spline systematic error was estimated as the median difference between the b-spline and the PCA-normalized (masked) spectrum in bins matching the breakpoint spacing. This error was typically of order 1% of the shot noise in the data; it exceeded the formal

¹⁴ See <http://ucolick.org/~xavier/IDL/>.

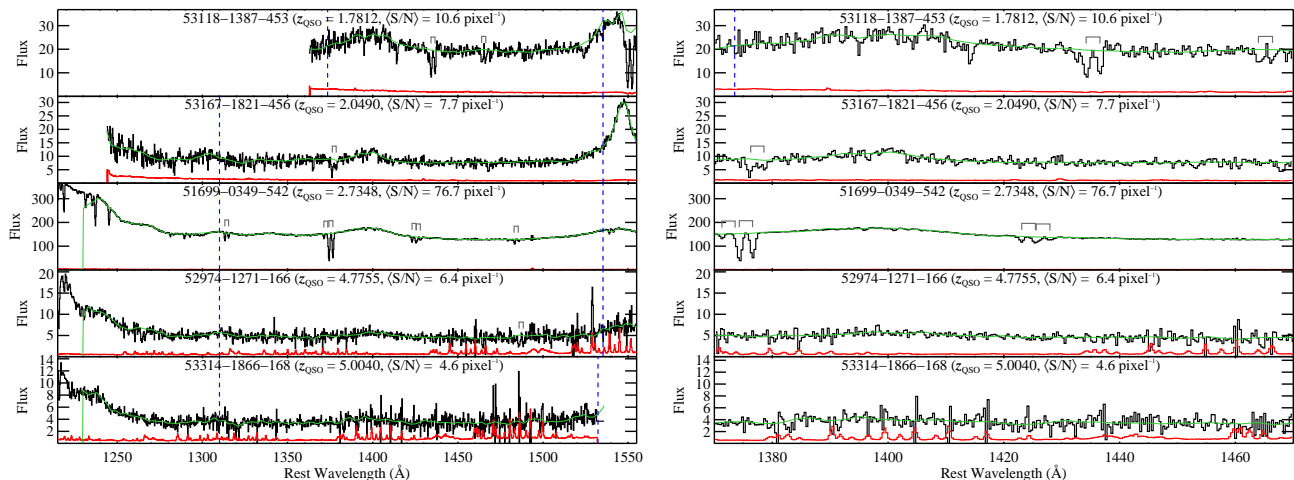


Figure 2. Examples of automated continuum fits. Several QSO spectra (black) and $1\text{-}\sigma$ error (red) are shown with their automated continuum fits (green). On the left are the full spectra, and a zoom of the central wavelength range is given on the right. All spectra were fit for $\lambda_r \geq 1230 \text{ \AA}$ with SDSS eigenspectra. For $\langle S/N \rangle \geq 8 \text{ pixel}^{-1}$ spectra, the eigen-fit was adjusted with a b-spline fit to the normalized spectrum. We surveyed the spectra for C IV absorbers between the (blue) vertical lines, which are outside the O I, Si II “forest” and more than 3000 km s^{-1} blueward of the QSO. The gray brackets indicate real C IV doublets from the final sample.

PCA fit error, and we added the two in quadrature to produce a total continuum error.

The sigma clipping methods described above are effective at identifying narrow features, instrumental artifacts, or defects in the spectra. However, they are not always optimal for finding true absorption lines, which are always below the continuum; they can also be kinematically complex and bias the fit. Since we have prior information about the characteristic widths of cosmological absorption, we develop methods in §2.3 to machine-identify candidate absorption lines with these characteristics for the actual survey. We ran each PCA-normalized spectrum through a single pass of the absorption-line finder, using the resulting catalogs to generate a master absorption mask for final hybrid-continuum fitting.

The full procedure for automated feature finding is described in §2.3; briefly, we convolve both the data and error arrays with the instrumental response profile, and search for absorption features with signal-to-noise ratio ≥ 3.5 per resolution element. For $\langle S/N \rangle \leq 16 \text{ pixel}^{-1}$ spectra, we masked out all such features; in high- S/N cases, we also enforced that the unconvolved spectral pixels at the line center must deviate from the continuum by $> 5\sigma$. Pixels falling within $\pm 600 \text{ km s}^{-1}$ of such features were added to the exclusion set. The mask consisting of automatically identified absorption lines was fed into the hybrid-continuum fit as a static mask.

This procedure produced excellent continuum fits for the vast majority of spectra. When it failed, the most common reasons were: poorly measured z_{QSO} , strong intrinsic absorption, broad-absorption lines, and foreground emission-line galaxy spectra superimposed on the quasar spectra. Instead of fixing these cases interactively, which would compromise our objective methodology and continuum error estimates, we chose to leave them in the sample and let the effects be accounted in our automated completeness and contamination tests (see §3).

2.3. Automated Candidate Selection

We limited our candidate search to C IV doublets where two automatically detected lines were within $\pm 150 \text{ km s}^{-1}$ of the characteristic velocity separation $\delta v_{\text{C IV}} = 498 \text{ km s}^{-1}$. The large uncertainty cut allowed heavily blended lines into our candidate list, but it also made the Mg II doublet our largest contaminant since $\delta v_{\text{Mg II}} = 767 \text{ km s}^{-1}$.

Our automated feature-finding algorithm is based on Prochter et al. (2006). The hybrid-normalized flux and error arrays were convolved with a Gaussian kernel with full-width at half-maximum equivalent to a resolution element of the SDSS spectrograph, i.e., $\sigma_{\text{C}} = 1 \text{ pixel}$. The error array included the continuum fit error. The regions where the convolved signal-to-noise $(S/N)_{\text{conv}}$ is greater than or equal to 3.5 per resolution element were identified as absorption features and saved to the sightline’s line list. We masked out the few pixels ($\approx 5 \text{ \AA}$) around the strong skylines at 5579 \AA and 6302 \AA .

Candidate C IV doublets were compiled by pairing automatically detected lines with the characteristic velocity separation $\delta v_{\text{C IV}} \pm 150 \text{ km s}^{-1}$ and by identifying isolated, automatically detected lines that were broad enough to be a candidate doublet by themselves. As discussed in §2.1, the search region is set so that the C IV candidate is redward of the O I, Si II “forest” ($\lambda_r \geq 1310 \text{ \AA}$) and blueward of the QSO by 3000 km s^{-1} . For any un-paired line, we re-ran the automated feature-finder with a $2.5\sigma_{\text{conv}}$ cut-off and searched for a partner candidate 1550 \AA line.

To identify isolated, broad lines that should be candidate C IV doublets, we used the automated procedure for measuring wavelength bounds (described in §2.4) to find lines with widths $\delta v_{\text{lin}} \geq 1.5 \delta v_{\text{C IV}}$.

Ultimately, we identified 29,789 candidates, 6,346 of which were from the broad-line search.

2.4. Measuring Absorber Properties

The redshift, equivalent width, and column density of a line depend on the definition of its wavelength bounds.

The bounds were automatically defined by where the convolved signal-to-noise array stopped decreasing from the perspective of the automatically detected centroid, and the bounds were not allowed to exceed the midpoint between themselves and neighboring lines. Thus, for C IV lines, the inner wavelength bounds were not allowed to exceed the midpoint of the doublet.

The redshift, equivalent width, and column density errors included the estimated error due to the hybrid-continuum. Redshifts were measured from the flux-weighted centroids. Equivalent widths were measured by simply summing the absorbed flux within the bounds.

We used the apparent optical depth method (AODM; Savage & Sembach 1991) to estimate column densities. Systems that are saturated (discussed below) formally have column densities that are lower limits (binary flag $f_N = 2$). Column density measurements that are less than $3\sigma_N$ are flagged as upper limits ($f_N = 4$).

With doublets, we have two measurements of the column density, and we use both to set N_{CIV} , as done in Cooksey et al. (2010). For doublets where both lines are measurements (not limits), N_{CIV} is the inverse-variance weighted mean of the two values. If one line is a measurement, N_{CIV} is set to its value. The column density *limit* is set to the inverse-variance weighted mean when both doublet limits are the same kind. When the doublet limits bracket a range, N_{CIV} is set to the un-weighted average with an error that reflects the range ($f_N = 8$). In the remaining cases, N_{CIV} is set to the better measurement/limit and flagged $f_N = 16$.

The AODM systematically overestimates the true column densities in low-S/N spectra (Fox et al. 2005). On the other hand, most doublets that can be detected in the low-resolution SDSS spectra are saturated, as evidenced by the doublet ratios of near unity; therefore, the AOD column densities would formally be lower limits. We define the doublet to be unsaturated when the equivalent width ratio $W_{\text{r},1548}/W_{\text{r},1550} > 2 - \sigma_{\text{R}}$, where σ_{R} is the ratio error due to the uncertainties in the measured equivalent widths. All other doublets are flagged as saturated with column densities that are lower limits; by this criterion, approximately 84% of the final catalog are saturated (see Table 3).

2.5. Interactive Doublet Verification

The candidate C IV selection relied solely on the characteristic wavelength separation of the doublet. However, true, unblended C IV doublets have a well-defined doublet ratio $W_{\text{r},1548}/W_{\text{r},1550}$ in the range of one to two in the saturated and unsaturated regimes, respectively. The resolved profiles of the doublet lines are very similar in the absence of blending. Most C IV absorbers are associated with Ly α absorption, though “naked” systems may exist (Schaye et al. 2007). There are frequently other metal lines associated with the C IV absorption, such as the Si IV and/or Mg II doublets. In addition, outside of the Ly α (and O I, Si II) forest, line confusion and blending are less severe, and the C IV doublet is one of the more common metal lines.

We developed a graphical user interface to present all this information for each system to assist us in rating the 29,789 candidates. We leveraged our experience with C IV absorption systems and the varying amounts of information available, depending on redshift, to assign

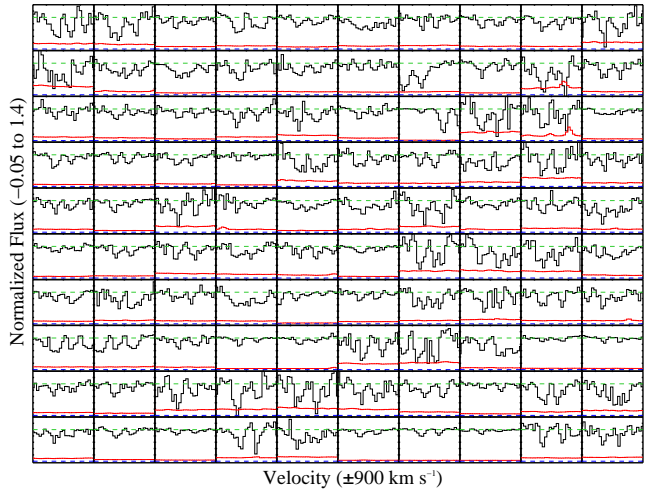


Figure 3. Example of C IV absorbers. One hundred doublet profiles are plotted from -900 km s^{-1} to 900 km s^{-1} with respect to the center of the doublet and from -0.05 to 1.4 in normalized flux units. The flux is shown in black and the $1\text{-}\sigma$ error in red. The horizontal dashed lines indicate the flux at unity (green) and zero (blue).

each candidate a rating:

0. definitely false—either can definitively identify the lines as other metal lines or as spurious bad pixels masquerading as absorption;
1. likely false—though cannot name alternate metal-line identification, better data would probably confirm this as not C IV absorption;
2. likely true—though sparse supporting evidence (e.g., associated lines), better data would probably confirm this as C IV absorption; or
3. definitely real—associated with other lines and/or shows clear correlations in line profiles.

A single author was trusted to accurately assign ratings of 0 or 3; these doublets were not viewed again. The more ambiguous cases (ratings 1 and 2) were reviewed by at least one additional author until consensus was achieved. We grouped the doublets into systems with $\delta v_{\text{abs}} < 250 \text{ km s}^{-1}$.

Though we excluded the BAL QSOs from Shen et al. (2011), we found several sightlines with strong, self-blended, highly blueshifted C IV absorbers. Since we focused on the *intergalactic* absorption systems, we excluded these 138 sightlines from further analysis and labeled them “visual BAL” QSOs in Table 2 (binary flag $f_{\text{BAL}} = 12$). In addition, the extremely strong absorption lines in these spectra corrupted the automated continuum fitting algorithm.

The final catalog includes all doublets with rating ≥ 2 . From the initial 29,789 candidates, 743 were in sightlines excluded as visual BAL QSOs. In the remaining 29,046 candidates, we found 16,459 real C IV doublets (see Table 3). A sample of doublets are shown in Figure 3. Ultimately, we analyzed the 14,772 with $\delta v_{\text{QSO}} < -5000 \text{ km s}^{-1}$ (see §4.1).

We assessed the effects of blending and bad continua by inspecting 4500 doublets chosen at random. We flagged doublets where the 1548, 1550, or both lines were blended or otherwise problematic (e.g., the bounds were unrealistic) and where the continua ought to be adjusted locally

(e.g., due to strong absorption or neighboring emission lines). The majority of our analysis depended on $W_{r,1548}$, so it mattered most what fraction of the 1548 lines were troublesome.

Over 90% of the random sample had “perfect” treatment of the 1548 line, and over 95% had acceptable continuum fits. The problematic doublets showed some redshift dependence due to the confused nature in the sky line region $\lambda_{\text{obs}} \gtrsim 7500 \text{ \AA}$ or $z_{1548} \gtrsim 3.8$, where the fraction of problematic 1548 lines jumped from $\approx 10\%$ to $\approx 20\%$. The stronger lines ($W_{r,1548} \gtrsim 2 \text{ \AA}$) were more often blended. These systems tended to be self-blended and would generally be problematic to surveys using box-car summation for equivalent widths, such as ours. To maintain the largely automated, and hence objective and repeatable, nature of the survey, we decided to accept the imperfections and assess the strength of our results in light of them.

3. COMPLETENESS TESTS

We test our survey completeness by generating a library of synthetic profiles, randomly distributing them in a subset of the sightlines, and tracking which simulated doublets were recovered. The goal was to populate a grid of doublet redshifts and rest equivalent widths with the fraction of recovered and accepted simulated doublets in each grid cell. We aimed to sample the full distribution of completeness limits so that we could leverage the large number of sightlines; for example, two spectra with 50% completeness in one (W_r, z_{1548}) cell are equivalent to one sightline with 100% completeness for the same parameters (Matejek & Simcoe 2012). In this section, we detail how we generated synthetic profiles, input and recover them, and measure the completeness, in addition to discussing biases.

3.1. Simulated Doublets

We parameterized the simulated doublets to produce absorption lines that look like the diversity of profiles observed in the SDSS spectra. We created a Voigt profile library with a uniform distribution of equivalent widths, since we aimed to generate uniform errors on detection completeness as a function of $W_{r,1548}$. Each component had a column density that was sampled linearly from $11 < \log N_{\text{CIV}} < 14$ and a Doppler parameter randomly selected in the range $5 \text{ km s}^{-1} < b < 40 \text{ km s}^{-1}$. For each system, one primary component was generated, and a random draw from a Poisson distribution, with mean of $\mu_{\text{comp}}^{\text{Pois}}$, determined the number of additional components for the system. The velocity offset for each component was drawn from a Gaussian distribution with standard deviation $\sigma_{\delta v}^{\text{Gauss}}$, clipped to keep all components within the maximum offset δv_{max} relative to the system redshift.

The bulk of our profiles were generated with $\mu_{\text{comp}}^{\text{Pois}} = 4$ or 7, $\sigma_{\delta v}^{\text{Gauss}} = 100 \text{ km s}^{-1}$, and $\delta v_{\text{max}} = 300 \text{ km s}^{-1}$, which were roughly based on the component properties measured by Boksenberg et al. (2003). However, to reproduce the diversity of profiles found in the SDSS data, we had to modify the parameters (e.g., larger $\mu_{\text{comp}}^{\text{Pois}}$ and δv_{max}), and we limited the alternate parameters to the larger equivalent width regime (e.g., $W_r \geq 1.2 \text{ \AA}$), where Boksenberg et al. (2003) did not have many systems.

We generated over 10^5 Voigt profiles. Then we randomly selected or duplicated (in extreme equivalent width regimes) profiles to uniformly sample $0.05 \text{ \AA} < W_{r,1548} < 3.25 \text{ \AA}$ in bins of 0.05 \AA , resulting in a library of 32,000 profiles.

3.2. Monte Carlo Procedures

We have two Monte Carlo completeness tests, referred to as basic and user. The basic test included all of the automated procedures, from continuum fitting to candidate selection. It was applied to the largest fraction of sightlines ($\approx 30\%$). We tested the user bias by visually inspecting the candidates in $\approx 6\%$ of the sightlines. The subsamples were set by requiring at least one sightline in each bin of $\Delta z_{\text{QSO}} = 0.25$ for $z_{\text{QSO}} \geq 1.7$ and $\Delta \langle S/N \rangle = 0.25 \text{ pixel}^{-1}$ for $\langle S/N \rangle \geq 4 \text{ pixel}^{-1}$. For the basic test, with more sampled sightlines, we kept sampling from the sightlines in these Δz_{QSO} and $\Delta \langle S/N \rangle$ bins, so that the bins with more sightlines had more tested for completeness. Extra high-redshift sightlines were included in the user test to increase the statistics.

We chose to input the simulated doublets into the actual spectra in order to sample realistic data. We “cleaned” each spectrum by removing a random 30% of the automatically detected absorption features. The flux between the wavelength bounds (see §2.4) was replaced by continuum with a scatter drawn from neighboring pixels, and the new error reflected those same pixels. By leaving the remaining absorption features in, we were able to measure the effects of blending and of absorption lines on the automated continuum fit and line-finding algorithm.

We set a fiducial absorber redshift density $dN_{\text{CIV}}/dz = 5$ to determine how many simulated doublets to input into the cleaned spectrum. This translated to typically injecting one to three doublets per loop, and the test iterated until at least 1000 simulated doublets were input per sightline. We did not change the error array when injecting profiles, which slightly but systematically lowered the signal-to-noise ratio of the simulated doublets.

For every sightline in the basic test, a random sample of profiles were drawn from our library and assigned redshifts to fall within the limits of the current sightline. The spectrum was “cleaned” to start and every 50th loop thereafter. We injected one to three simulated doublets, fit the hybrid-continuum (see §2.2), and ran the automated candidate identification algorithm (see §2.3). Any injected profile was flagged as recovered if the automatically identified candidate bounds spanned the observed wavelength of the simulated system. For any profile that was *not* recovered, we measured the flux-weighted redshift, equivalent width, and AOD column density at the expected location. The input and recovered information was stored for later processing (see §3.3).

The user completeness test served a dual purpose. It tested the effects of human bias (e.g., we were less likely to accept real doublets at high redshift due to poor sky subtraction at $\gtrsim 7000 \text{ \AA}$) and our accepted false-positive rate (i.e., how often we rated non-C IV lines as C IV absorption). The steps were largely the same for one sightline in the user test as in the basic, but we “cleaned” the profile every iteration and an author rated the automatically detected candidates. However, we modified

Table 3
C IV System Summary

(1)	(2)	(3)	(4)	(5)	(6)	(7)	(8)
QSO ID	z_{QSO}	z_{1548}	$W_{r,1548}$ (Å)	$W_{r,1550}$ (Å)	$C(W_{r,1548})$	$\log N_{\text{C IV}}$ ($\log(\text{cm}^{-2})$)	f_N
52143-0650-199	1.8449	1.52755	0.567 ± 0.147	0.981 ± 0.162	0.562 ± 0.206	$> 14.30 \pm 0.14$	3
52143-0650-178	2.6404	2.23461	0.425 ± 0.059	0.303 ± 0.058	0.363 ± 0.092	$> 14.10 \pm 0.06$	3
		2.43947	1.050 ± 0.078	0.653 ± 0.072	0.860 ± 0.023	$> 14.53 \pm 0.03$	3
52902-1091-546	2.5551	2.34348	0.734 ± 0.202	0.898 ± 0.198	0.713 ± 0.192	$> 14.75 \pm 0.14$	3
		2.42902	1.053 ± 0.191	0.733 ± 0.196	0.860 ± 0.066	$?14.63 \pm 0.20$	7
51791-0387-093	1.8973	1.77015	0.388 ± 0.097	0.479 ± 0.098	0.305 ± 0.132	$> 14.01 \pm 0.13$	3
52235-0750-550	2.6383	2.16695	0.581 ± 0.123	0.594 ± 0.127	0.576 ± 0.161	$> 14.23 \pm 0.09$	3
54389-2822-423	2.7668	2.36223	0.738 ± 0.087	0.332 ± 0.088	0.716 ± 0.073	14.34 ± 0.06	1
54327-2630-423	2.7251	2.23946	0.489 ± 0.100	0.390 ± 0.102	0.458 ± 0.151	$> 14.16 \pm 0.11$	3
54452-2824-554	2.5566	2.08349	0.837 ± 0.040	1.050 ± 0.042	0.781 ± 0.025	$> 14.55 \pm 0.02$	3
		2.08788	0.971 ± 0.039	0.398 ± 0.039	0.836 ± 0.014	14.46 ± 0.02	1
		2.14618	0.769 ± 0.041	0.462 ± 0.037	0.738 ± 0.030	$> 14.39 \pm 0.03$	3
		2.21361	0.381 ± 0.039	0.254 ± 0.041	0.294 ± 0.059	$> 14.00 \pm 0.05$	3
		2.38185	0.395 ± 0.039	0.284 ± 0.039	0.317 ± 0.062	$> 14.05 \pm 0.05$	3
52143-0650-561	1.7593	1.63718	0.393 ± 0.049	0.185 ± 0.053	0.314 ± 0.075	13.99 ± 0.07	1
52991-1489-581	1.8536	1.69764	1.013 ± 0.090	0.812 ± 0.088	0.849 ± 0.030	$> 14.55 \pm 0.04$	3
52203-0685-567	2.0921	1.70301	1.165 ± 0.186	0.669 ± 0.180	0.877 ± 0.038	14.57 ± 0.08	1
		1.75102	0.875 ± 0.121	0.827 ± 0.122	0.799 ± 0.070	$> 14.54 \pm 0.07$	3

Note. — For each sightline (identified in Columns 1 and 2), every confirmed doublet is listed by the redshift of its C IV 1548 line (Column 3). The rest equivalent widths of the C IV lines are given in Columns 4 and 5. In Column 6, we give the completeness fraction for the doublet from the whole survey average. The C IV column density (Column 7) is the combined value from the AODM measurements in both lines. The binary column density flag f_N is composed of: 1 = good to analyze; 2 = lower limit; 4 = upper limit; 8 = un-weighted average; and 16 = default to line value with greater significance (Column 8). (This table is available in a machine-readable form in the online journal. A portion is shown here for guidance regarding its form and content.)

the simulated doublets to have an unphysical characteristic wavelength separation of 4.8 \AA or 924 km s^{-1} so that any candidate was most likely either simulated or spurious. The fake $\lambda\lambda 1547, 1552$ profile library was truncated to $W_{r,1547} \leq 1 \text{ \AA}$. We did not simulate other absorption lines because, fundamentally, we are conducting a blind C IV survey.

3.3. Completeness Correction and Unblocked Co-Moving Path Length

We combined the completeness tests in bins of redshift and onto grids of equivalent width so that we correct any detected absorber based on its completeness fraction. The estimated completeness fraction for a given grid point (z_g, W_g) is simply $N_{\text{accept}}/N_{\text{input}}$, the fraction of input C IV doublets that are recovered automatically and accepted by the user, in the given grid cell. The two completeness tests separately measured the recovering and accepting effects so that the final completeness fraction is estimated by:

$$C(z_g, W_g) = \frac{N_{\text{rec}}(z_g, W_g) N_{\text{accept}}(z_g, W_g)}{N_{\text{input}}(z_g, W_g) N_{\text{rec}}(z_g, W_g)}, \quad (1)$$

where the right-hand product can be thought of as $C_{\text{basic}}C_{\text{user}}$. The completeness grid $C(z_g, W_g)$ collapses to a curve $C(W_g)$ in a fixed redshift bin. The basic completeness uncertainty $\sigma_{C_{\text{basic}}}$ is estimated by the Wilson score interval for a binomial distribution (Wilson 1927). This confidence interval estimator is well behaved for small N_{input} and/or for extreme completeness fractions.

The statistics on the user completeness were naturally smaller than for the basic, so we fit $C_{\text{user}}(W_r)$ with the following model:

$$C_{\text{user}}(W_r) = C_0(1 - e^{\beta(W_r - W_0)}) \quad (2)$$

in two redshift bins. The dividing $z = 2.97$ corresponded to the beginning of the sky line region at $\approx 7000 \text{ \AA}$, with its resulting decrease in C_{user} due to confusion, and matched the start of the highest redshift bin. The fit uncertainties were estimated from Monte Carlo re-sampling of the equivalent-width errors, and the final error on $C(W_r)$ was propagated from $\sigma_{C_{\text{basic}}}$ and $\sigma_{C_{\text{user}}}$. We extrapolated the fits to larger equivalent widths when we calculated the full completeness fraction. The user completeness test is discussed in detail in §3.4 below.

We scaled $C(z_g, W_g)$ by the fraction of the total path length *not* obscured by doublets with greater equivalent widths, in the redshift bin. All C IV lines blocked $< 2\%$ of the total survey path length (see Table 2).

In actuality, N_{input} and N_{rec} contain the information only for the profiles and sightlines actually sampled in the basic completeness test. Any sightline that did not have a measurement for one or more quantities was accounted for with the average of the sightlines actually tested in the requested Δz_{QSO} and $\Delta \langle S/N \rangle$ bin.

The unblocked co-moving path length¹⁵ for each grid cell is calculated by simply multiplying the completeness fraction by the total path length available in each redshift bin:

$$\begin{aligned} \Delta X(W_g) &= \Delta X(z_g)C(z_g, W_g) \\ \sigma_{\Delta X(W_g)}^2 &= \Delta X(z_g)^2 \sigma_{C(z, W)}^2. \end{aligned} \quad (3)$$

In Figure 4, the black curves are the grid values $\Delta X(W_g)$ and errors.

The unblocked co-moving path length to which our survey is sensitive for any given detected equivalent width

¹⁵ The co-moving path length is related to redshift as follows: $X(z) = 2\sqrt{\Omega_M(1+z)^3 + \Omega_\Lambda}/(3\Omega_M)$.

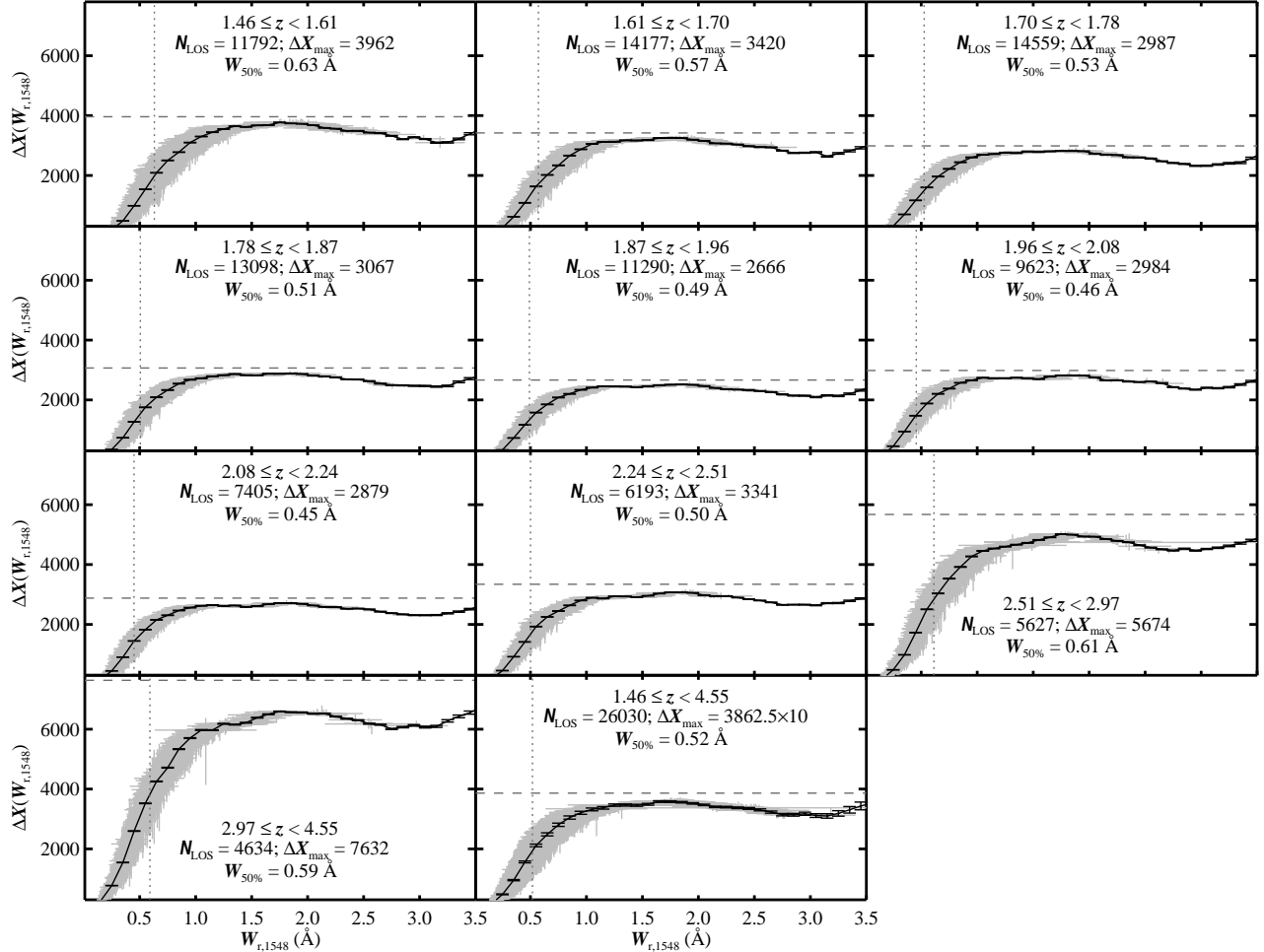


Figure 4. Results from Monte-Carlo completeness tests. The completeness-corrected co-moving path length as a function of rest equivalent width $\Delta X(W_{r,1548})$ is shown for the 11 redshift bins used in the current study. The black curve and errors are the completeness curves (Equation 3), and the gray points and errors are the observations (Equation 4). The horizontal, dashed line traces the maximum path length available in the bin, and the vertical, dotted line indicates the equivalent width where we are 50% complete.

W_i is interpolated from the grid of $\Delta X(W_g)$:

$$\begin{aligned} \Delta X(W_i) &= \text{interpol}(\Delta X(W_g), W_g, W_i) \\ \sigma_{\Delta X}^2 &= \text{interpol}(\sigma_{\Delta X}^2(W_g), W_g, W_i) + \\ &\quad \left(\Delta X(W_i) - \Delta X(W_i \pm \sigma_{W_i}) \right)^2. \end{aligned} \quad (4)$$

The error on $\Delta X(W_i)$ accounts for the error in our completeness correction ($\sigma_{\Delta X}$) and for the uncertainty in our equivalent width measurement (σ_{W_i}). We plot each doublet’s $\Delta X(W_{r,1548})$ in gray in Figure 4. Clearly, the uncertainty in equivalent width dominates the error in the completeness correction.

In all redshift bins, the typical completeness fraction reached 50% by $W_{r,1548} \approx 0.6 \text{ \AA}$, a value we frequently use as the minimum in subsequent analyses.

3.4. Automated and Interactive Biases

The completeness curves do not monotonically increase to 100% at large equivalent width (see Figure 4). Instead, they roll off at $W_{r,1548} \approx 2 \text{ \AA}$. This feature results from the incompleteness in the broad (self-blended) C IV search and, to a much lesser extent ($< 5\%$), from broad

profiles being over-fit by the continuum algorithm, which led them to being missed in the automated search.

The user completeness test measured our ability to correctly rate real, automatically detected doublets (“true positives”) as well as the rate at which we include spurious pairs of lines as true doublets (“accepted false negatives”). We injected $\mathcal{N}_{\text{input}} = 5021$ fake doublets with $W_r < 1 \text{ \AA}$ and $\delta v_{\text{QSO}} < -5000 \text{ km s}^{-1}$, and $\mathcal{N}_{\text{rec}} = 3070$ were automatically recovered. Of these, we correctly rated $\mathcal{N}_{\text{accept}} = 2489$. The left panels of Figure 5 show the trends of the user completeness with redshift, spectrum $\langle S/N \rangle$, and equivalent width.

Generally, C_{user} decreases with increasing redshift and decreasing $\langle S/N \rangle$. Sky lines become numerous at $\lambda \gtrsim 7000 \text{ \AA}$, and poor sky subtraction leaves features in the spectrum that mimic absorption lines (see Figure 2). In the visual verification step, a larger fraction of real doublets are rejected due to the severe confusion. Lower signal-to-noise spectra induces the same effect.

There were an additional 966 spurious candidates brought forth by the automated search, of which we incorrectly accepted 121. The accepted false-positive fraction peaks at $\approx 20\%$ at $z \approx 3$ and $\langle S/N \rangle \approx 10$. However,

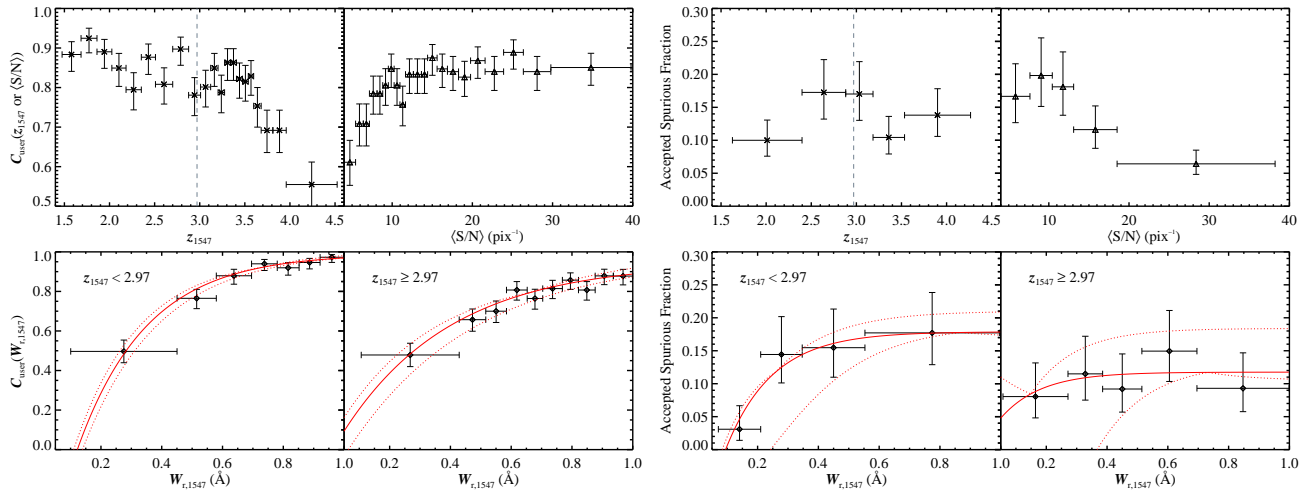


Figure 5. Biases of visual verification and trends of spurious detections. *Left:* We tested the “user bias” by rating fake $\lambda\lambda 1547, 1552$ doublets that were injected and automatically recovered as candidates. The four panels show the completeness of our ability to correctly rate true doublets, as a function of redshift, spectrum (S/N), and equivalent width in two redshift bins. The redshift cut (vertical line) was determined by the decrease in $C_{\text{user}}(z_{1547})$ due to the sky-line region at $\approx 7000 \text{ \AA}$ and by the highest redshift SDSS bin. The (red) solid and dashed lines are the best-fit model (see Equation 2) and its $1\text{-}\sigma$ errors. *Right:* At the same time, we estimated the accepted false-positive fraction as functions of redshift, signal-to-noise, and equivalent width. These spurious pairs of lines were *not* injected but were automatically recovered. The lower panels show the best-fit model and errors to the accepted spurious fraction over $W_{r,1547}$.

our acceptance fraction grows sharply at $W_r \lesssim 0.6 \text{ \AA}$ and plateaus to 18% and 12% for $z < 2.97$ and ≥ 2.97 , respectively. The estimated co-moving line densities of accepted false positives with $W_r \geq 0.6 \text{ \AA}$ are $d\mathcal{N}_{\text{afp}}/dX = 0.022$ and 0.020 for the low and high redshift bins, respectively.

We detail how we applied corrections for the accepted false-positive rate in the next section.

4. RESULTS

The bulk of the analysis of the C IV sample was performed either on the whole dataset or in bins in redshift space. The bins were determined empirically from the $\delta v_{\text{QSO}} < -5000 \text{ km s}^{-1}$ sample to have about 1500 doublets per bin, and the δv_{QSO} cut is explained below.

4.1. Frequency Distribution

The equivalent width frequency distribution $f(W_r)$ is the number of detections $\mathcal{N}_{\text{obs}}(W_r)$ per rest equivalent width bin ΔW_r per the total co-moving path length available, in the given equivalent width bin, $\Delta X(W_r)$:

$$f(W_r) = \frac{\mathcal{N}_{\text{obs}}(W_r)}{\Delta W_r \Delta X(W_r)} \quad (5)$$

$$\sigma_{f(W_r)}^2 = f(W_r)^2 \left(\left(\frac{\sigma_{\mathcal{N}_{\text{obs}}}}{\mathcal{N}_{\text{obs}}(W_r)} \right)^2 + \left(\frac{\sigma_{\Delta X}}{\Delta X(W_r)} \right)^2 \right).$$

The error on \mathcal{N}_{obs} is estimated from a Poisson distribution if $\mathcal{N}_{\text{obs}} < 120$ and from a Gaussian approximation if $\mathcal{N}_{\text{obs}} \geq 120$. For $\Delta X(W_r)$ and $\sigma_{\Delta X}$, we used Equation 4 with the center of the equivalent width bin being W_i and $\sigma_{W_i} = 0.5\Delta W_r$.

We used the maximum likelihood analysis of Cooksey et al. (2010) to fit $f(W_r)$ with an exponential:

$$f(W_r) = k e^{\alpha W_r} \quad (6)$$

(see Figure 6). The normalization k and scale α were simultaneously fit, and the errors were estimated by the

maximum extent of the $1\text{-}\sigma$ error ellipse on the likelihood surface (see Figure 7). All frequency distributions were fit over the range $0.6 \text{ \AA} \leq W_{r,1548} \leq \max[W_{r,1548} + \sigma_{W_r}]$. The results were not strongly dependent on the choice of the upper limit. The exponential model is a very good description of the data, and the best-fit parameters are given in Table 4.

The best-fit parameters show smooth redshift evolution with respect to the constant $d\mathcal{N}_{\text{CIV}}/dX$ curves in Figure 7. The co-moving line density is simply the integral of the frequency distribution from some limiting equivalent width W_{lim} to infinity, and substituting in our exponential model, we see:

$$\left. \frac{d\mathcal{N}_{\text{CIV}}}{dX} \right|_{\text{fit}} = \frac{-k}{\alpha} e^{\alpha W_{\text{lim}}}. \quad (7)$$

By fixing $d\mathcal{N}_{\text{CIV}}/dX$, we can solve for the required normalization k for any given α . The $1\text{-}\sigma$ ellipses are elongated in the direction of the constant $d\mathcal{N}_{\text{CIV}}/dX$ curves, and redshift evolution can be seen by tracking systematic change perpendicular to these curves. The lowest five redshift bins ($1.46 \leq z < 1.96$) fall along roughly the same constant $d\mathcal{N}_{\text{CIV}}/dX$ curve. The next three highest redshift bins ($1.96 \leq z < 2.51$) have slightly smaller line densities. Then there is almost a factor of two drop over the highest two redshift bins ($2.51 \leq z < 4.55$).

Since the accepted false-positive rate is essentially constant at $W_r \geq 0.6 \text{ \AA}$ (see §3.4), the frequency distribution of accepted false positives is a scaled-down version of the measured frequency distribution. Therefore, we scale the original $f_0(W_r)$ as follows:

$$f(W_r) = \left(1 - \frac{d\mathcal{N}_{\text{afp}}/dX}{d\mathcal{N}_{\text{CIV}}/dX} \right) f_0(W_r) \quad (8)$$

and propagate the errors. This results in a decrease of $\approx 6\%$ to 12% , depending on the redshift. For the exponential fits, we scale the best-fit normalization k_0 in a

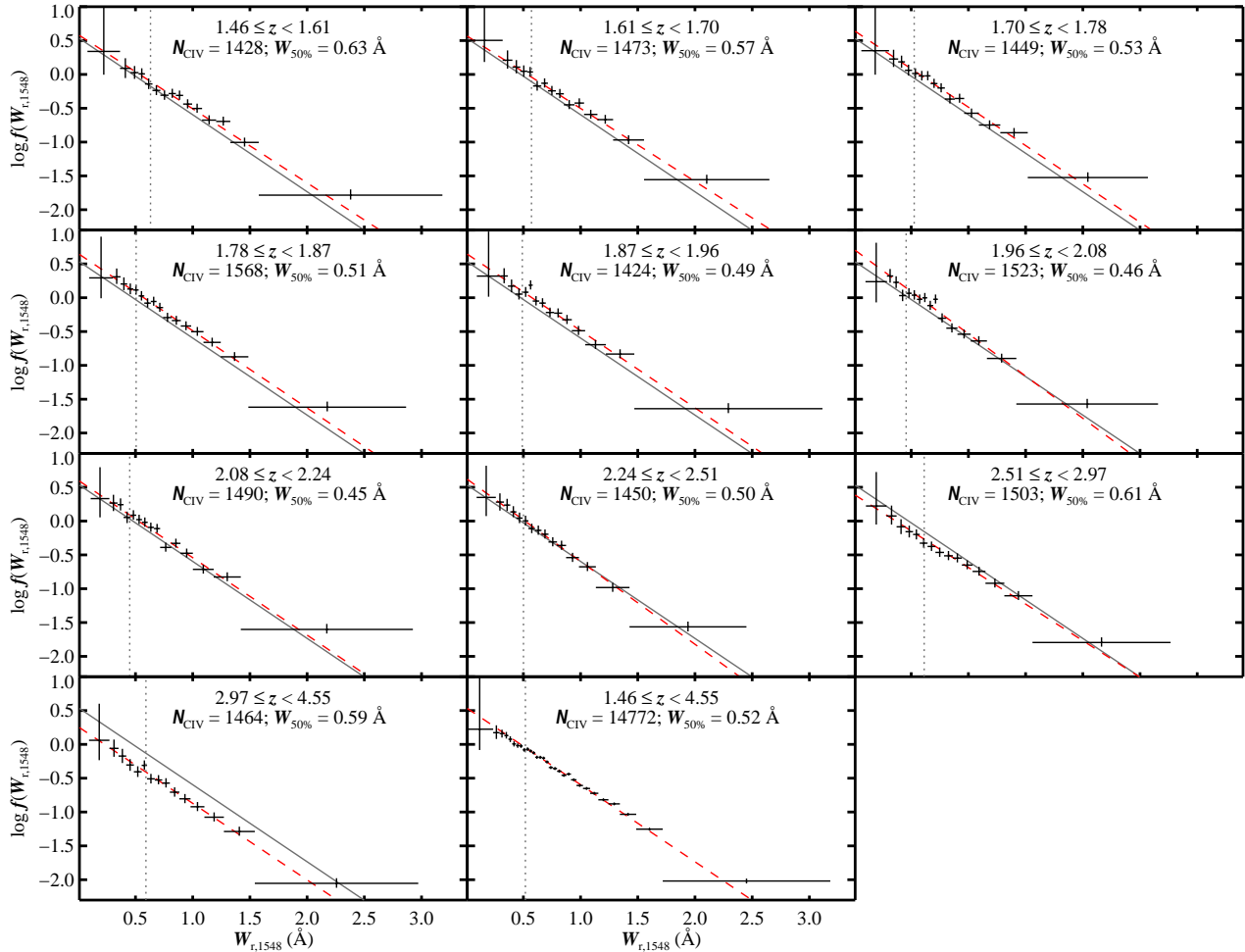


Figure 6. Equivalent width frequency distributions. The maximum likelihood fits of an exponential function are the dashed (red) lines, for each redshift bin, and the solid (gray) line, for the full sample. There is little evolution with redshift. The observations have been completeness corrected, and the redshift-specific 50% completeness limits are the vertical dotted lines.

similar fashion:

$$k = \left(1 - \frac{dN_{\text{afp}}/dX}{(dN_{\text{CIV}}/dX)_{\text{fit}}}\right) k_0, \quad (9)$$

but the denominator is the integrated line density from the exponential model (Equation 7). We report the propagated errors in Table 4 and in the text. However, since we cannot compute the change in the likelihood surface, we only shift the ellipses in Figures 7 and 8.

4.1.1. Effect of Blending and “Intrinsic” Absorbers

As mentioned in §2.5, blended profiles are an issue for this survey, which relies on automated procedures and boxcar summation to measure equivalent widths. We ran 1000 Monte Carlo simulations to estimate the net effect of blending. There were over 10^6 (17%) simulated doublets recovered in the completeness tests that had measured equivalent widths more than 3σ larger than the input value, indicative of blending. We measured the median ($\langle W_{\text{blend}} \rangle = 0.2 \text{ \AA}$) and standard deviation ($\sigma_{W_{\text{blend}}} = 0.5 \text{ \AA}$) of the distribution, where $W_{\text{blend}} = W_{\text{r,rec}} - (W_{\text{r,input}} + 3\sigma_{W_{\text{r,rec}}})$. For each realization, we tested the worst-case scenario by decreasing the equivalent width of a random 20% of the absorbers,

which was the largest blended fraction estimated in §2.5. The magnitude of the decrease was drawn randomly from the half of a Gaussian distribution below its mean, set to $\langle W_{\text{blend}} \rangle$, with standard deviation $\sigma_{W_{\text{blend}}}$. Then, the new sample was fit with an exponential $f(W_{\text{r}})$ model. The median best-fit parameters from these Monte Carlo simulations were in very good agreement with those in Table 4, and the standard deviation of the Monte Carlo results were ten-times smaller than the quoted uncertainties. These simulations assessed the worst-case scenario, by taking the largest estimated fraction of blended lines (see §2.5) and only decreasing the equivalent widths (as opposed to also re-sampling the the other 80% of the doublets).

In addition, the completeness corrections account for blending since we compiled the curves in Figure 4 with respect to the *measured*—as opposed to input—equivalent widths. There were other absorption lines in the spectra, and the randomly placed simulated profiles were blended at a realistic rate, as seen by the agreement of the blended fraction from our visual estimate (§2.5) and from the 10^6 simulated doublets described above. Thus, our results are robust to the effects of blending.

We tested the effect of the δv_{QSO} cut on our results by increasing δv_{QSO} and re-fitting the full red-

Table 4
 C IV Results Summary

(1)	(2)	(3)	(4)	(5)	(6)	(7)	(8)	(9)	(10)	(11)	(12)
$\langle z \rangle$	z_{lim}	N_{obs}	ΔX_{max}	$W_{50\%}$ (\AA)	dN_{CIV}/dz	dN_{CIV}/dX	Ω_{CIV} ($\times 10^{-8}$)	N_{fit}	k (\AA^{-1})	α (\AA^{-1})	χ^2_{red}
1.96274	[1.46623, 4.54334]	14772	38624	0.52	$0.92^{+0.02}_{-0.01}$	$0.275^{+0.004}_{-0.004}$	$1.71^{+0.20}_{-0.20}$	8918	$3.49^{+0.31}_{-0.30}$	$-2.62^{+0.04}_{-0.04}$	0.577
1.55687	[1.46623, 1.60986]	1428	3962	0.63	$0.95^{+0.03}_{-0.03}$	$0.332^{+0.011}_{-0.010}$	$2.18^{+0.39}_{-0.39}$	1025	$3.87^{+0.94}_{-0.82}$	$-2.52^{+0.11}_{-0.12}$	1.560
1.65971	[1.61004, 1.69993]	1473	3420	0.57	$1.00^{+0.04}_{-0.03}$	$0.336^{+0.012}_{-0.011}$	$2.10^{+0.32}_{-0.32}$	956	$3.77^{+0.95}_{-0.82}$	$-2.48^{+0.12}_{-0.13}$	0.876
1.73999	[1.70035, 1.78000]	1449	2987	0.53	$1.08^{+0.04}_{-0.04}$	$0.356^{+0.013}_{-0.012}$	$2.17^{+0.28}_{-0.28}$	902	$4.46^{+1.24}_{-1.06}$	$-2.61^{+0.14}_{-0.13}$	1.672
1.82360	[1.78007, 1.86985]	1568	3067	0.51	$1.09^{+0.04}_{-0.04}$	$0.351^{+0.012}_{-0.012}$	$2.11^{+0.23}_{-0.24}$	932	$4.49^{+1.20}_{-1.04}$	$-2.63^{+0.13}_{-0.13}$	1.291
1.91460	[1.87000, 1.95998]	1424	2665	0.49	$1.12^{+0.04}_{-0.04}$	$0.355^{+0.013}_{-0.012}$	$2.15^{+0.23}_{-0.23}$	824	$4.53^{+1.28}_{-1.09}$	$-2.63^{+0.14}_{-0.14}$	1.832
2.01778	[1.96002, 2.07997]	1523	2983	0.46	$1.04^{+0.04}_{-0.04}$	$0.322^{+0.012}_{-0.011}$	$1.86^{+0.17}_{-0.17}$	852	$5.18^{+1.76}_{-1.51}$	$-2.87^{+0.15}_{-0.15}$	2.838
2.15320	[2.08009, 2.23997]	1490	2878	0.45	$1.04^{+0.04}_{-0.04}$	$0.312^{+0.012}_{-0.011}$	$1.92^{+0.17}_{-0.17}$	807	$4.01^{+1.21}_{-1.04}$	$-2.63^{+0.14}_{-0.14}$	3.267
2.35608	[2.24015, 2.50914]	1450	3341	0.50	$0.96^{+0.03}_{-0.03}$	$0.276^{+0.011}_{-0.010}$	$1.61^{+0.18}_{-0.18}$	775	$4.26^{+1.62}_{-1.37}$	$-2.82^{+0.15}_{-0.16}$	1.296
2.72298	[2.51028, 2.96976]	1503	5673	0.61	$0.83^{+0.03}_{-0.03}$	$0.221^{+0.009}_{-0.008}$	$1.44^{+0.22}_{-0.22}$	969	$2.48^{+0.74}_{-0.65}$	$-2.49^{+0.12}_{-0.12}$	0.837
3.25860	[2.97005, 4.54334]	1464	7632	0.59	$0.59^{+0.02}_{-0.02}$	$0.145^{+0.006}_{-0.005}$	$0.87^{+0.13}_{-0.13}$	876	$1.82^{+0.75}_{-0.65}$	$-2.61^{+0.13}_{-0.13}$	1.548

Note. — Summary of the most common redshift bins and data used for the various analyses. Columns 1–2 give the median, minimum, and maximum redshifts for the observed number of doublets (Column 3), and the maximum co-moving pathlength in the redshift bin is given in Column 4. The 50% completeness limit from the Monte Carlo tests is in Column 5. The redshift and co-moving absorber line densities for $W_r \geq 0.6 \text{ \AA}$ are in Columns 6–7. In Column 8, the Ω_{CIV} from summing the mass in the $W_r \geq 0.6 \text{ \AA}$ absorbers is a lower limit, since the majority of absorbers are saturated. The frequency distribution was fit with an exponential $f(W_r) = k \exp(\alpha W_r)$ for N_{fit} absorbers with $W_r \geq 0.6 \text{ \AA}$ (Column 9), and the best-fit parameters are given in Columns 10–11. The reduced χ^2 from the best fit and $f(W_r)$ (in bins with ≈ 100 doublets each) is given in Column 12.

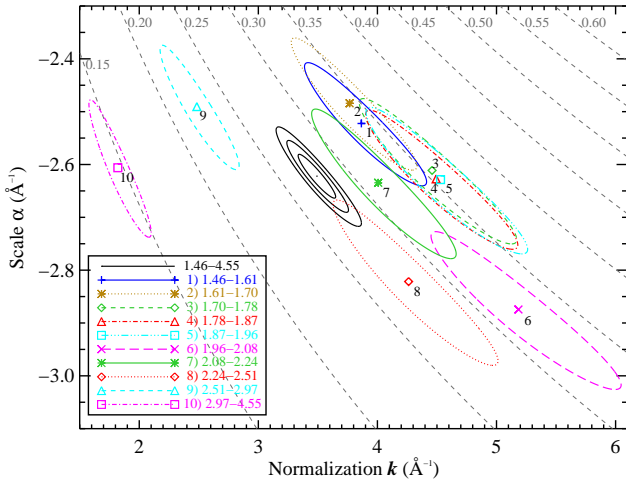


Figure 7. Best-fit $f(W_r)$ parameters and errors. We fit the frequency distribution with an exponential function (see Equation 6). The best-fit normalization k and scale α and the $1\text{-}\sigma$ error ellipses are plotted for the ten small redshift bins (numbered points); the 1, 2, and $3\text{-}\sigma$ contours are shown for the fit to the full sample (black ellipses). The best-fit parameters smoothly evolve with redshift, as seen by comparing the ellipses with the constant dN_{CIV}/dX curves (gray, dashed lines).

shift sample (see Figure 8). Systems close to the background QSO could potentially be high velocity, intrinsic absorbers and/or affected by quasar clustering, enrichment, and/or local ionization. The general trend for $\delta v_{\text{QSO}} < -4000 \text{ km s}^{-1}$ is decreasing normalization (i.e., k) with nearly constant shape (α). The decrease in k is due to the number of absorbers decreasing faster than the path length up to at least $\delta v_{\text{QSO}} = -15000 \text{ km s}^{-1}$. For example, with $\delta v_{\text{QSO}} = -10000 \text{ km s}^{-1}$, we have 17.5% less path length but 25% fewer $W_r \geq 0.6 \text{ \AA}$ doublets. This trend is partially explained by quasars residing in dense environments (e.g., Prochaska et al. 2011), where the chance of intersecting a metal-enriched galaxy halo

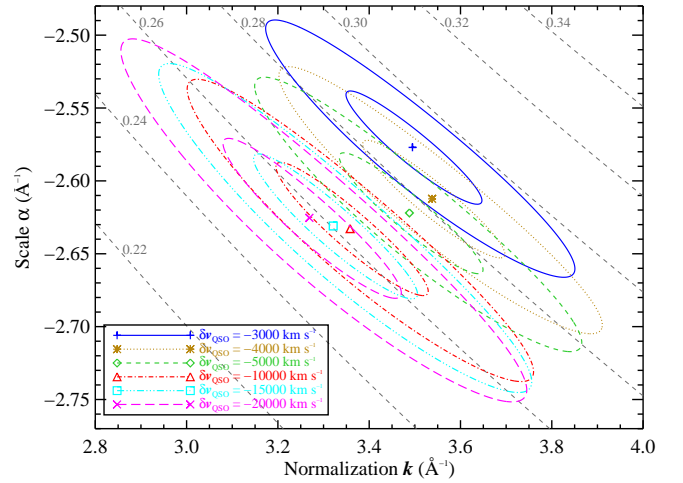


Figure 8. Best-fit $f(W_r)$ parameters for different δv_{QSO} values. We tested the effects of the δv_{QSO} cut on the fit to the full C IV sample. The contours are 1 and 3σ , and the gray, dashed lines are constant dN_{CIV}/dX curves. We adopt $\delta v_{\text{QSO}} = -5000 \text{ km s}^{-1}$ for the main analyses.

is increased.

However, this effect would not dominate out to $\delta v_{\text{QSO}} = -10000 \text{ km s}^{-1}$. The lack of “convergence” at very large δv_{QSO} may be partially due to poorly measured quasar redshifts. Hewett & Wild (2010) re-measured the majority of the redshifts for the Schneider et al. (2010) DR7 QSOs, with better automated routines. Adopting the Hewett & Wild (2010) redshifts affects over 80% of the total 16,459 C IV systems. The majority of the quasar redshifts *increased*, with a median $\langle \delta v_{\text{em}} \rangle = 381 \text{ km s}^{-1}$, standard deviation 764 km s^{-1} , and maximal extent $-4200 \text{ km s}^{-1} \lesssim \delta v_{\text{em}} \lesssim +5700 \text{ km s}^{-1}$. In addition, there are redshift-dependent fluctuations in δv_{em} . Using the Hewett & Wild (2010) redshifts would affect our analysis; however, the change in the total sam-

ple size, given a δv_{QSO} cut, is less than 2%. Given this small fraction and the incompleteness of the new redshifts, we chose to continue with the Schneider et al. (2010) redshifts, but we adopt $\delta v_{\text{QSO}} = -5000 \text{ km s}^{-1}$ for the bulk of our analyses which reduces the sample to 14,772 doublets.

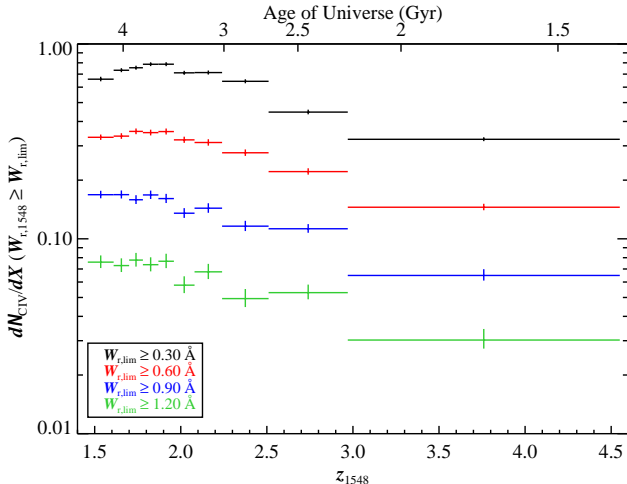


Figure 9. Co-moving C IV line density evolution. The number of absorbers per co-moving path length increases steadily and consistently from $z_{1548} = 4.5 \rightarrow \approx 1.74$. As expected from the nearly unchanging nature in the shape of $f(W_r)$ (see Figure 6), there is little dependence on $W_{r,\text{lim}}$, noting that we are typically 50% at $W_r \approx 0.6 \text{ \AA}$.

4.2. C IV Absorber Line Density

We directly measured the absorber line density for doublets with $W_r \geq W_{\text{lim}}$ as follows:

$$\frac{dN_{\text{CIV}}}{dX}(W_r \geq W_{\text{lim}}) = \frac{\mathcal{N}_{\text{C}}(W_r)}{\Delta X(z)} \quad (10)$$

$$\sigma_{dN/dX}^2 = \left(\frac{\sigma_{\mathcal{N}_{\text{C}}}}{\Delta X(z)} \right)^2.$$

The completeness-corrected number of absorbers in any given bin is the completeness-weighted sum of the observed absorbers in the bin:

$$\mathcal{N}_{\text{C}}(W_r) = \sum_{W_i \geq W_r - 0.5\Delta W_r}^{W_i < W_r + 0.5\Delta W_r} \frac{1}{C(W_i)} \quad (11)$$

$$\sigma_{\mathcal{N}_{\text{C}}}^2 = \sigma_{\mathcal{N}_{\text{obs}}}^2 + \sum_{W_i \geq W_r - 0.5\Delta W_r}^{W_i < W_r + 0.5\Delta W_r} \left(\frac{\sigma_{\mathcal{C}}(W_i)}{C(W_i)^2} \right)^2.$$

Again, \mathcal{N}_{obs} is the contribution of the actual observed number of absorbers in the given W_r bin, and the completeness-corrected number $\mathcal{N}_{\text{C}} \geq \mathcal{N}_{\text{obs}}$. The error $\sigma_{\mathcal{N}_{\text{obs}}}$ is estimated from a Poisson distribution if $\mathcal{N}_{\text{obs}} < 120$ and from a Gaussian approximation if $\mathcal{N}_{\text{obs}} \geq 120$.

We subtract $d\mathcal{N}_{\text{afp}}/dX$ from all quoted dN_{CIV}/dX values, in the appropriate redshift bins (see §3.4) and add the errors in quadrature. For $W_r \geq 0.6 \text{ \AA}$, $d\mathcal{N}_{\text{afp}}/dX = 0.020_{-0.002}^{+0.003}$ ($1.4 < z < 4.6$); $0.022_{-0.004}^{+0.005}$ ($z < 2.97$); and $0.020_{-0.003}^{+0.004}$ ($z \geq 2.97$).

We present dN_{CIV}/dX for different equivalent width limits in Figure 9. The line density shows little differential evolution based on $W_{r,\text{lim}}$, as expected from the consistent shape of the frequency distributions over time (Figure 6). For $W_r \geq 0.6 \text{ \AA}$, the inverse-variance weighted average $dN_{\text{CIV}}/dX = 0.350 \pm 0.005$ for $1.46 \leq z < 1.96$ (or the lowest five redshift bins). This average is 2.37 ± 0.09 times larger than the highest redshift dN_{CIV}/dX at $z = 3.76$. Though the magnitude of the increase is modest, the detection is a $> 20\sigma$ result. Thus, the line density grows consistently and smoothly from $z_{1548} = 4.5 \rightarrow \approx 1.74$, then plateaus at $dN_{\text{CIV}}/dX \approx 0.34$ until $z = 1.46$, as expected from the best-fit $f(W_r)$ parameters (see Figure 7).

There is a known bias in the SDSS quasar color selection that leads to an excess of Lyman-limit systems at $3 \lesssim z_{\text{QSO}} \lesssim 3.5$ (Prochaska et al. 2010; Worseck & Prochaska 2011), which likely increases the incidence of strong metal-line absorption systems at these redshifts. Therefore, there is potential for the decrease in the highest SDSS bin to be even larger, but the effect of the color selection on the C IV sample is beyond the scope of this paper.

4.3. Comparison with Previous Results

To fairly compare to other surveys, we applied various W_r cuts to our complete sample, chosen to match the corresponding cuts of prior surveys.

To compare $f(W_r)$, we converted published column density frequency distributions *fits* from Songaila (2001) and D’Odorico et al. (2010) to equivalent width frequency distributions by assuming the linear curve of growth and mapping $f(N_{\text{CIV}})$ directly to $f(W_{r,1548})$: $f(W_r) = f(N_{\text{CIV}})dN_{\text{CIV}}/dW_r$. We adjusted for cosmology as necessary. A single-component cloud becomes saturated and nonlinear at $\log N_{\text{CIV}} \approx 14$, which translates to $W_{r,1548} \approx 0.6 \text{ \AA}$, where we typically are $\approx 50\%$ complete.

While we have good statistics on the rare, strong absorbers, we suffer from incompleteness at $W_r \lesssim 0.6 \text{ \AA}$. Songaila (2001) and D’Odorico et al. (2010) were smaller, higher-resolution, higher-S/N studies, and they were complete to very low W_r but suffered from sample variance at larger equivalent widths. However, Figure 10 shows that our results are consistent with each other in the overlap region. Our best-fit parameters to the exponential $f(W_r)$ in the D’Odorico et al. (2010) and Songaila (2001) redshift bins were, respectively: $\alpha = -2.65_{-0.04}^{+0.04} \text{ \AA}^{-1}$ and $k = 3.72_{-0.35}^{+0.37} \text{ \AA}^{-1}$ for $1.6 \leq z \leq 3.6$ with 7884 systems; and $\alpha = -2.58_{-0.13}^{+0.13} \text{ \AA}^{-1}$ and $k = 2.29_{-0.69}^{+0.80} \text{ \AA}^{-1}$ for $2.9 \leq z \leq 3.54$ with 878 systems.

We compared the SDSS redshift and co-moving line densities with the literature (Steidel 1990; Barlow & Tytler 1998; Cooksey et al. 2010; D’Odorico et al. 2010; Simcoe et al. 2011). For D’Odorico et al. (2010), we used their best-fit $f(N_{\text{CIV}})$ values to calculate dN_{CIV}/dX and $dN_{\text{CIV}}/dz = (dN_{\text{CIV}}/dX)(dX/dz)$ for $\log N_{\text{CIV}} \geq 14$. For Barlow & Tytler (1998) and Steidel (1990), we estimated $dN_{\text{CIV}}/dX = (dN_{\text{CIV}}/dz)(dX/dz)^{-1}$. The Steidel (1990) results match ours well for the range where the author was fairly complete but with $\approx 20\%$ uncertainty, compared to our $\approx 2\%$ errors (see Figure 11). Extending

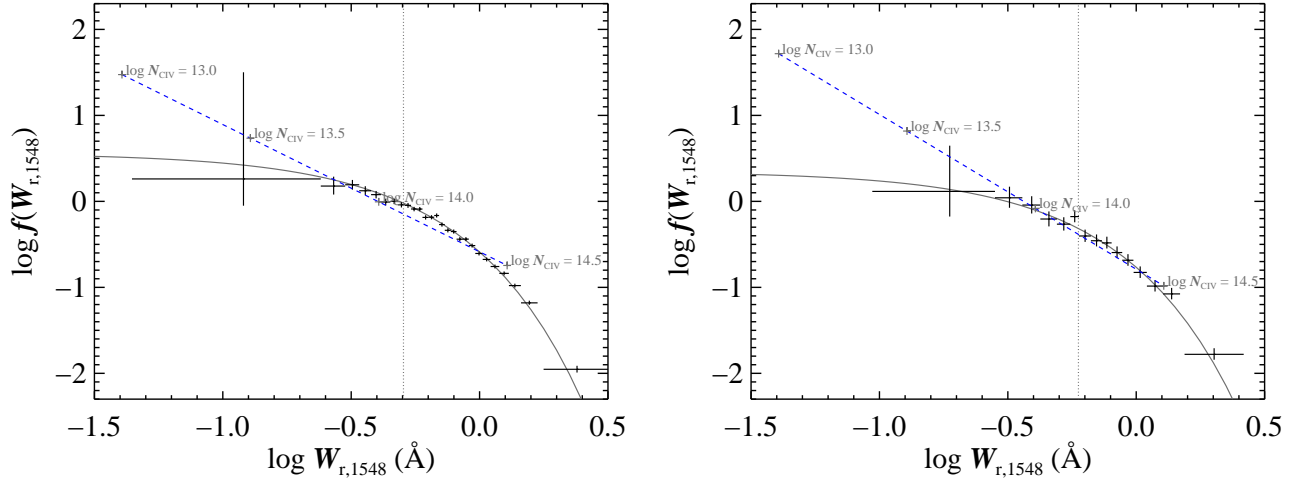


Figure 10. Comparing $f(W_r)$ to smaller, higher resolution studies. We show the best power-law fit from *left*: $1.6 \leq z \leq 3.6$ ($\alpha_{\text{pl}} = -1.71 \pm 0.07$; D’Odorico et al. 2010) and *right*: $2.9 \leq z \leq 3.54$ ($\alpha_{\text{pl}} = -1.8 \pm 0.1$; Songaila 2001) as the (blue) dashed lines. Our best exponential fit for each redshift bin is shown on top of the observed $f(W_r)$ (in bins of ≈ 500 and 100, respectively). The vertical 50%-complete line also happens to be around where a single C IV *component* saturates. The gray plus-signs indicate the equivalent widths where the labeled column densities fall.

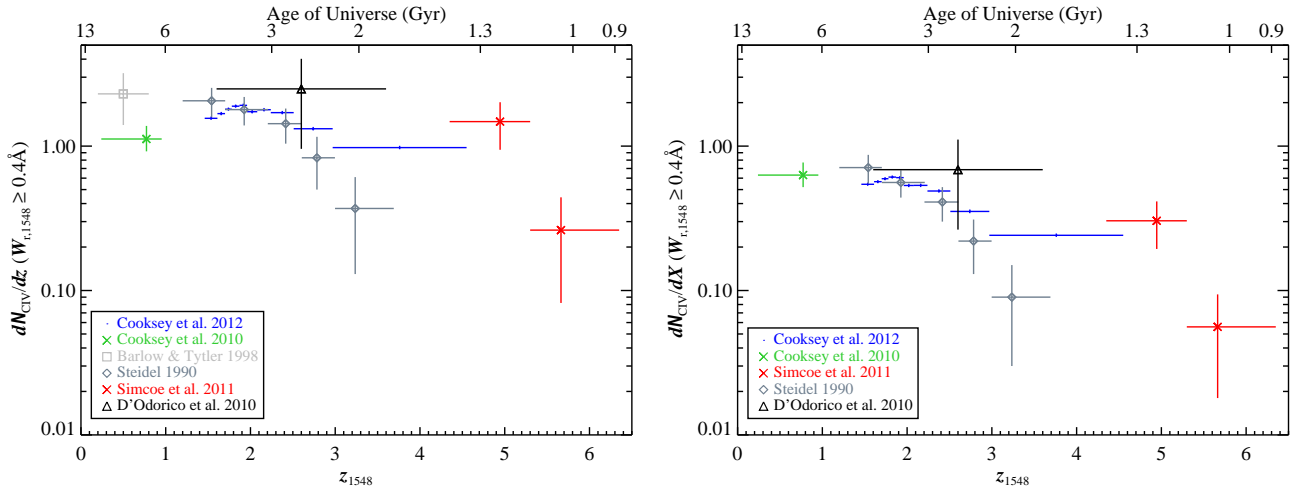


Figure 11. Redshift (left) and co-moving (right) C IV absorber line densities. We compare apples-to-apples dN_{CIV}/dz with $W_r \geq 0.4 \text{ \AA}$ with five surveys: Barlow & Tytler (1998, light gray square), Cooksey et al. (2010, green cross), D’Odorico et al. (2010, black triangle), Steidel (1990, gray diamonds), and Simcoe et al. (2011, red crosses). The co-moving line density steadily increases from high to low redshift. The growth in dN_{CIV}/dX indicates a consistent increase with time in the product of the co-moving number density and the physical cross-section of the absorbing clouds.

the redshift coverage by including the low-redshift measurements of Barlow & Tytler (1998) and Cooksey et al. (2010) and the high-redshift values from Simcoe et al. (2011), we see that dN_{CIV}/dX has steadily increased by, roughly, a factor of ten from $z_{1548} = 6 \rightarrow 0$.

5. DISCUSSION

5.1. C IV Evolution

We show the best measurements of dN_{CIV}/dX for $W_r \geq 0.6 \text{ \AA}$ and $0 < z < 6.5$ in the top panel of Figure 12.¹⁶ The co-moving line density relates to the co-moving

¹⁶ For $z < 1$, we summed the eight $W_r \geq 0.6 \text{ \AA}$ systems in the *HST* sample (Cooksey et al. 2010) to get $dN_{\text{CIV}}/dX = 0.63^{+0.14}_{-0.11}$. For $z > 4$, we have $dN_{\text{CIV}}/dX = 0.212 \pm 0.092$ for $z = 4.94$ (2

volume density of absorbing clouds n_{com} and their physical cross-section σ_{phys} :

$$\frac{dN_{\text{CIV}}}{dX} = \frac{c}{H_0} n_{\text{com}} \sigma_{\text{phys}}. \quad (12)$$

Thus, the roughly order-of-magnitude increase in dN_{CIV}/dX from high-to-low redshift means the product $n_{\text{com}} \sigma_{\text{phys}}$ has increased by a factor of ≈ 10 . We know the metallicity of the universe has steadily increased over cosmic time, so the possible number of C IV-absorbing clouds (i.e., n_{com}) has likely increased. At least some C IV absorption traces galaxy halos at low (Chen et al. 2001) and high redshift (Adelberger et al. 2005; Martin

systems) and 0.026 ± 0.027 for $z = 5.66$ (1) from the FIRE sample (Simcoe et al. 2011).

et al. 2010; Steidel et al. 2010). Since galaxies (and their halos) have likely grown over cosmic time, increases in both σ_{phys} and n_{com} appear to contribute to the increase in dN_{CIV}/dX .

Adelberger et al. (2005) reported that almost all $\log N_{\text{CIV}} \geq 14$ absorbers arise within ≈ 80 kpc of Lyman-break galaxies (LBGs) at $2 \lesssim z \lesssim 3$. The evidence included: individual strong absorber-LBG pairs; strong absorption in stacked spectra of close background galaxies, shifted to the rest-frame of the foreground galaxies; and similar LBG-C IV cross-correlation and LBG autocorrelation functions, suggesting they have the same spatial distribution.

Steidel et al. (2010) increased the LBG-LBG pairs for stacking analysis, and they measured average $W_{r,1548} = 0.13 \pm 0.05 \text{ \AA}$ and $1.18 \pm 0.15 \text{ \AA}$ at distances $b = 63$ kpc and 103 kpc, respectively. Interpolating between these two measurements, an average $W_{r,1548} = 0.6 \text{ \AA}$ system would reside at $b \approx 85$ kpc. The Steidel et al. (2010) LBG sample went as faint as $\approx 0.3 L^*$, assuming the luminosity function of Reddy & Steidel (2009), and since they used stacks of galaxy spectra, their analysis included the effects of partial covering fractions.

Since the $W_r \geq 0.6 \text{ \AA}$ C IV absorbers in our sample have $\log N_{\text{CIV}} \gtrsim 14$, we used the co-moving number density of UV-selected galaxies, to estimate the typical galaxy-C IV cross-section over time with Equation 12. We measured $n_{\text{com,UV}}$ with the UV luminosity functions from Oesch et al. (2010), Reddy & Steidel (2009) and Bouwens et al. (2007), which covered several smaller redshift bins spanning $0.5 < z < 2$, $1.9 < z < 3.4$, and $3.8 \lesssim z \lesssim 5.9$, respectively. For each luminosity function, we integrated the best-fit Schechter function down to $0.5 L^*$ or ≈ 0.75 mag fainter than the published M_{UV}^* , which ranged between ≈ -19 and -21 mag. We estimated the $n_{\text{com,UV}}$ errors with Monte Carlo simulations.

The UV-selected galaxy number density, $n_{\text{com,UV}}$, may increase by a factor of two to three from $z \approx 6 \rightarrow 0$, but the uncertainties are large (see Figure 12, middle panel). Applying $n_{\text{com,UV}}$ and dN_{CIV}/dX to Equation 12, we estimated σ_{phys} , the physical galaxy-C IV cross-section (Figure 12, lower panel). For some redshift bins, multiple luminosity functions could be used in conjunction with our dN_{CIV}/dX , and we show all resulting values but highlight the preferred values with filled symbols.

The galaxy-C IV cross-section shows no evolution over the SDSS redshift range within the errors, which are dominated by the 20%–60% uncertainties in $n_{\text{com,UV}}$. Assuming the cross-section is due to a spherical halo that projects with 100% C IV covering fraction, the halo radius would be $R_{\text{phys}} = \sqrt{\sigma_{\text{phys}}/\pi} \approx 50$ kpc for $1.5 \lesssim z \lesssim 4.5$. This distance agrees with Adelberger et al. (2005) and allows for e.g., a non-unity covering fraction or limiting to brighter UV-selected galaxies, both of which would increase R_{phys} .

There is an approximately 10-fold increase in σ_{phys} from $z \approx 6 \rightarrow 0$ when we include the dN_{CIV}/dX measurements from Simcoe et al. (2011) and Cooksey et al. (2010), respectively. This increase in the galaxy-C IV cross-section is comparable to that of dN_{CIV}/dX over the same redshift range. Thus, if the $W_r \geq 0.6 \text{ \AA}$ C IV absorbers were only tracing galaxy halos, the redshift evolution of dN_{CIV}/dX could be solely due to the halos

filling up with triply-ionized carbon, through some combination of physical growth, increased metallicity, and/or evolution in the ionizing background.

However, the uncertainty in the $z < 1$ cross-section estimate is large and consistent with an increase of only two to three compared with the $z \approx 6$ value. In this case, the roughly order-of-magnitude increase in dN_{CIV}/dX could equally be due to modest increases in $n_{\text{com,UV}}$ and σ_{phys} .

We emphasize that the preceding discussion assumes all $W_r \geq 0.6 \text{ \AA}$ C IV systems at $0 < z < 6$ are only found in the circum-galactic media of UV-selected galaxies. Any intergalactic C IV contribution to dN_{CIV}/dX at any redshift would cause us to overestimate the galaxy-C IV cross-section.

Evolution in the ultraviolet background (UVB) possibly explains the seeming spike in σ_{phys} at $z \approx 5$. Simcoe (2011) showed that C IV is a preferred, if not dominant, transition of carbon at $z = 4.3$ compared to lower redshift, assuming the UVB of Haardt & Madau (2001) or Faucher-Giguère et al. (2009). Though the redshift window of this effect is small ($\Delta z \approx 0.5$), the increase in C IV-ionizing photons would increase the C IV cross-section of UV-selected galaxies and may explain the spike in dN_{CIV}/dX and σ_{phys} . In general, triply-ionized carbon increasingly becomes a disfavored transition of carbon with decreasing redshift, given a standard model of the UVB (Oppenheimer & Davé 2008; Simcoe 2011). The UVB likely dominates the ionization flux at the expected tens of kiloparsecs from the host galaxies. Thus, the increasing number of C IV absorbers towards lower redshift indicates an increasing enrichment of the gas, to more-than-compensate for the decreasingly favored triply-ionized state.

C IV absorption could also be a galactic wind signature (see Steidel et al. 2010). However, the dN_{CIV}/dX redshift evolution does not mimic the evolution of dN_{MgII}/dX for $W_{r,2796} \gtrsim 1 \text{ \AA}$ absorbers, and these strong Mg II doublets are often analyzed as wind tracers (Weiner et al. 2009; Rubin et al. 2010; Bordoloi et al. 2011, but also see Gauthier et al. 2010 and Kacprzak et al. 2011). Strong Mg II absorbers evolve strongly with redshift by increasing with increasing redshift (Nestor et al. 2005; Prochter et al. 2006), peaking at $z \approx 3$, and then decreasing at higher redshifts (?). The latter study showed that the evolution in dN_{MgII}/dX tracks the cosmic star-formation rate (Bouwens et al. 2010), using the scaling relation of Ménard et al. (2011), reinforcing the idea that strong Mg II absorbers arise in galactic winds.

We see no decrease at lower redshifts for strong C IV absorbers (see Figure 9). If strong C IV and Mg II absorbers were both tracing winds, then, to account for their different redshift evolution, either: they must probe outflows in different ways; or strong C IV absorption traces an additional medium, such as halo gas, that contributes significantly to its dN_{CIV}/dX evolution.

5.2. C IV Mass Density

The C IV doublet redshifts into optical passbands for $1.5 \lesssim z \lesssim 5.5$ and has been observed extensively with large, ground-based telescopes (Songaila 2001; Boksenberg et al. 2003; Schaye et al. 2003; Scannapieco et al. 2006; D’Odorico et al. 2010). Surveys of ultraviolet quasar spectra taken with *HST* cover the $z < 1$ C IV sys-

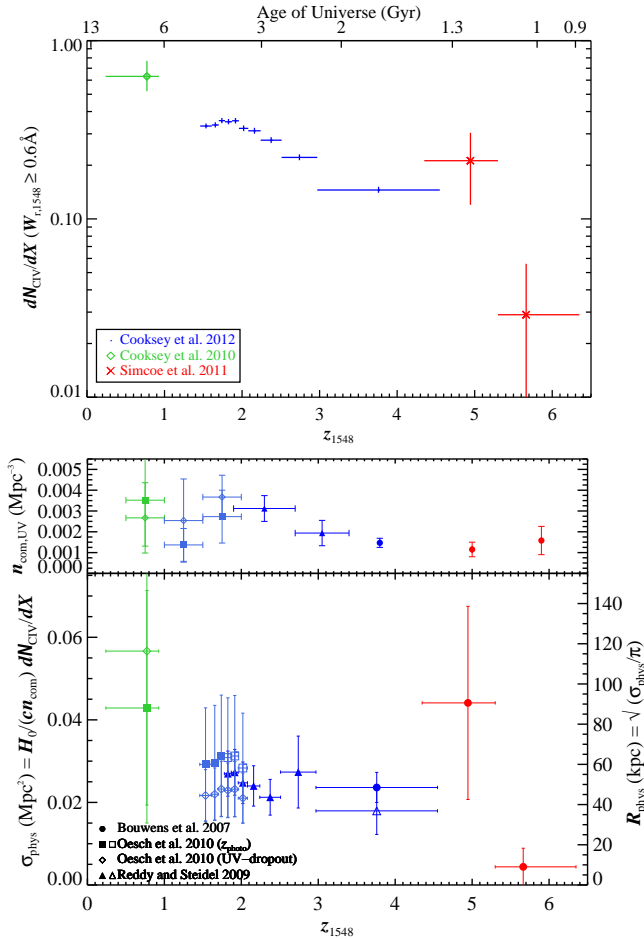


Figure 12. Evolving nature of C IV absorbers. *Top:* By combining the current SDSS values with those from Cooksey et al. (2010) and Simcoe et al. (2011), we show that dN_{CIV}/dX for $W_{r,1548} \geq 0.6 \text{ \AA}$ has increased 10-fold, roughly, from $z = 6 \rightarrow 0$. *Middle:* We calculated the co-moving number density of UV-selected galaxies by integrating the UV luminosity functions from Bouwens et al. (2007), Oesch et al. (2010), and Reddy & Steidel (2009), down to $0.5 L^*$. UV-selected galaxies are bright, star-forming galaxies, such as the LBGs that Adelberger et al. (2005) showed likely host most $\log N_{\text{CIV}} \geq 14$ absorbers at $2 \lesssim z \lesssim 3$. *Bottom:* Assuming that all $W_{r,1548} \geq 0.6 \text{ \AA}$ doublets are in UV-selected galaxy halos, we estimated the galaxy-C IV cross-section as a function of redshift with Equation 12. The inferred cross-sections from the SDSS $1.5 \lesssim z \lesssim 4.5$ sample are consistent with the area that Adelberger et al. (2005) and Steidel et al. (2010) measured.

tems (Danforth & Shull 2008; Cooksey et al. 2010). More recently, improved infrared spectrographs have pushed C IV surveys to $z \approx 6$ (Ryan-Weber et al. 2009; Becker et al. 2009; Simcoe et al. 2011). Typically these studies have focused on the evolution of Ω_{CIV} , the C IV mass density relative to the closure density. The first moment of the column density frequency distribution $f(N_{\text{CIV}})$ is related to Ω_{CIV} as follows:

$$\Omega_{\text{CIV}} = \frac{H_0 m_C}{c \rho_{c,0}} \int_{N_{\min}}^{N_{\max}} f(N_{\text{CIV}}) N_{\text{CIV}} dN_{\text{CIV}}, \quad (13)$$

where $H_0 = 71.9 \text{ km s}^{-1} \text{ Mpc}^{-1}$ is the Hubble constant today; $m_C = 2 \times 10^{-23} \text{ g}$ is the mass of the carbon atom; c is the speed of light; and the critical density

$\rho_{c,0} = 3H_0^2(8\pi G)^{-1} = 9.77 \times 10^{-30} \text{ g cm}^{-3}$ for our assumed Hubble constant.

The earliest (optical) studies found that Ω_{CIV} was relatively constant for $2 \lesssim z \lesssim 4.5$ (Songaila 2001; Boksenberg et al. 2003; Schaye et al. 2003; Songaila 2005; Scannapieco et al. 2006). Cooksey et al. (2010) showed that Ω_{CIV} increased by at least a factor of four from $z \approx 3$ to $z < 1$. Using better optical spectra, D’Odorico et al. (2010) found that Ω_{CIV} increased smoothly from $z = 3$ to $z = 1.5$ and mapped well onto the $z < 1$ values.

However, all these studies measured a power-law shape for the $f(N_{\text{CIV}})$, which formally corresponds to an infinite C IV mass density. These surveys were limited to small numbers of available sightlines, typically less than 50. The rarest systems are the strongest, and these dominate the mass density measurement when the distribution is a power law. Hence the small-number statistics on the strongest C IV absorbers limited the quoted Ω_{CIV} to be for $12 \lesssim \log N_{\text{CIV}} \lesssim 15$, with one survey pushing to $\log N_{\text{CIV}} \approx 16$ (Scannapieco et al. 2006). Indeed, scaling the Scannapieco et al. (2006) Ω_{CIV} to $\log N_{\text{CIV}} \leq 15$ reduces their value by 45% (Cooksey et al. 2010).

Our analysis, however, provides good statistics on the rare, strong systems, which dominate the SDSS sample. The observed Ω_{CIV} can be approximated by the sum of the detected C IV absorbers (Lanzetta et al. 1991). The total column density in a given redshift bin is simply:

$$N_{\text{tot}} = \sum_{N_{\text{obs}}} N_{\text{CIV}} \quad (14)$$

$$\sigma_{N_{\text{tot}}}^2 = \sigma_{N_{\text{obs}}}^2 + \sum_{N_{\text{obs}}} \sigma_{N_{\text{CIV}}}^2,$$

where, again, we factor in the counting uncertainty for the number of detections $\sigma_{N_{\text{obs}}}$. Then, we estimated the mass density relative to the critical density as:

$$\Omega_{\text{CIV}} = \frac{H_0 m_C}{c \rho_{c,0}} \frac{N_{\text{tot}}}{\langle \Delta X(W_r) \rangle} \quad (15)$$

$$\sigma_{\Omega}^2 = \Omega_{\text{CIV}}^2 \left(\left(\frac{\sigma_{N_{\text{tot}}}}{N_{\text{tot}}} \right)^2 + \left(\frac{\sigma_{\langle \Delta X \rangle}}{\langle \Delta X(W_r) \rangle} \right)^2 \right).$$

Since the completeness corrections were compiled in equivalent width space, we used the median $\Delta X(W_r)$ available to each of the absorbers in the given bin, and the error was the standard deviation of the detections. The small scaling to account for the accepted false-positive distribution follows that of the frequency distribution (Equation 8).

In Figure 13, we plot Ω_{CIV} over redshift from several studies for $\log N_{\text{CIV}} \geq 14$, adjusted for the new limits and cosmology (see Cooksey et al. 2010, for details). The direct SDSS measurements are *lower* limits since we have predominately saturated absorbers and use the AODM to estimate column densities. However, we can still exclude values below the limits, including the Songaila (2001) measurements at $z < 3$.¹⁷ This reinforces the D’Odorico et al. (2010) result that Ω_{CIV} smoothly increases. In an upcoming paper, we will be combining

¹⁷ Schaye et al. (2003) and Songaila (2005) used pixel optical depth methods to also measure Ω_{CIV} , but it is unclear how best to compare their values to our traditional quasar absorption-line study. For this reason, we omit discussion of their results.

the D’Odorico et al. (2010) and current datasets to fit $f(N_{\text{CIV}})$ and measure Ω_{CIV} for $\log N_{\text{CIV}} \gtrsim 12$ via Equation 13.

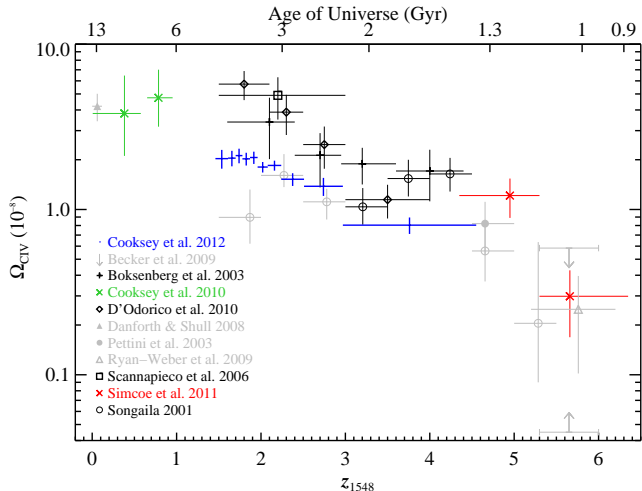


Figure 13. Redshift evolution of Ω_{CIV} for $\log N_{\text{CIV}} \geq 14$ absorbers. The SDSS apparent optical depth values are *lower limits* (blue), since most systems are saturated. However, these lower limits firmly exclude the $z < 3$ measurements from Songaila (2001), which have been grayed out with the other superseded measurements, and support the result that Ω_{CIV} smoothly increases from $z \approx 3$ to $z = 1.5$ from D’Odorico et al. (2010).

6. SUMMARY

We have completed the largest C IV survey to date by leveraging the SDSS DR7 quasar catalog (Schneider et al. 2010). In 26,030 sightlines with $z_{\text{QSO}} \geq 1.7$ and $\langle \text{S/N} \rangle \geq 4 \text{ pixel}^{-1}$, we identified 14,772 C IV systems at least 5000 km s^{-1} blueward of the quasar. The entire doublet catalog and other tools for analysis (e.g., completeness grids) are made available for the community.¹⁸

The bulk of the C IV survey was automated, from continuum fitting to candidate selection. We visually verified all doublets in the final catalog. Our Monte Carlo completeness tests included the effects of the automated algorithms, user bias, and accepted false positives. We analyzed the sample as a whole and in ten redshift bins of roughly 1500 doublets each. We also constructed and analyzed other subsamples as needed, for specific comparisons to published studies.

The equivalent width frequency distribution $f(W_r)$ is described well by an exponential model. The best-fit parameters evolved smoothly with redshift, with the largest change arising in the normalization. The parameter evolution follows the trend of increasing dN_{CIV}/dX with increasing redshift—a 2.37 ± 0.09 increase over $z = 4.55 \rightarrow \approx 1.74$. For $1.46 \leq z < 1.96$, $dN_{\text{CIV}}/dX \approx 0.34$.

In the region of overlap, the SDSS $f(W_r)$ agree well with the published column density frequency distributions $f(N_{\text{CIV}})$ from smaller, high-resolution, high-S/N surveys (Songaila 2001; D’Odorico et al. 2010). We converted $f(N_{\text{CIV}})$ to $f(W_r)$ assuming the linear curve-of-growth. The published $f(N_{\text{CIV}})$ distributions were best fit by a power-law formalism. Thus, combined with the

exponential nature of the strong-end of $f(W_r)$, we at last see an exponential cut-off in the equivalent width distribution that has not been previously characterized because of small sample sizes. The location of this cut-off sets the high-end range for C IV absorbers and formally leads to convergence in the cosmic C IV mass density.

In this paper, we joined our large sample of strong absorbers to the fits of weak absorbers obtained at high resolution. In a forthcoming paper, we will perform a joint analysis of our SDSS sample with the high-resolution data of D’Odorico et al. (2010) to fit clean forms to the full range of $f(N_{\text{CIV}})$. This will allow us to improve our understanding of the C IV mass density evolution, where currently our SDSS study only yields lower limits for $\log N_{\text{CIV}} \geq 14$ systems.

The co-moving line density dN_{CIV}/dX smoothly increases, approximately, ten-fold from $z = 6 \rightarrow 0$ for $W_{r,1548} \geq 0.6 \text{ \AA}$ absorbers. Physically, this means that the physical cross section (σ_{phys}) and/or co-moving number density of C IV absorbing clouds (n_{com}) has increased steadily over time, since dN_{CIV}/dX is proportional to their product. We estimated the projected C IV-absorbing cross-section of UV-selected galaxies to be $R_{\text{phys}} \approx 50 \text{ kpc}$, by assuming all the SDSS $W_r \geq 0.6 \text{ \AA}$ absorbers arise in $\geq 0.5 L^*$ galaxy halos, which is in good agreement with Adelberger et al. (2005) and Steidel et al. (2010).

This is the first paper in a series on various metal lines in the SDSS DR7 quasar spectra, which will provide a comprehensive and uniform collection of catalogs for future analysis and detailed comparison with cosmological hydrodynamic simulations.

We thank J. Harker, D. Ogden, J. Pritchard, and P. Creasey for their programming help and P. Jonsson for productive discussions regarding statistics and programming. We gratefully acknowledge the vital role of the Adam J. Burgasser Endowed Chair. The current study was funded largely by the National Science Foundation Astronomy & Astrophysics Postdoctoral Fellowship (AST-1003139) and in part by the MIT Department of Physics and the Alfred P. Sloan Foundation Research Fellowship.

Funding for the SDSS and SDSS-II has been provided by the Alfred P. Sloan Foundation, the Participating Institutions, the National Science Foundation, the U.S. Department of Energy, the National Aeronautics and Space Administration, the Japanese Monbukagakusho, the Max Planck Society, and the Higher Education Funding Council for England. The SDSS Web Site is <http://www.sdss.org/>.

The SDSS is managed by the Astrophysical Research Consortium for the Participating Institutions. The Participating Institutions are the American Museum of Natural History, Astrophysical Institute Potsdam, University of Basel, University of Cambridge, Case Western Reserve University, University of Chicago, Drexel University, Fermilab, the Institute for Advanced Study, the Japan Participation Group, Johns Hopkins University, the Joint Institute for Nuclear Astrophysics, the Kavli Institute for Particle Astrophysics and Cosmology, the Korean Scientist Group, the Chinese Academy of Sciences (LAMOST), Los Alamos National Laboratory, the

¹⁸ See <http://igmabsorbers.info/>.

Max-Planck-Institute for Astronomy (MPIA), the Max-Planck-Institute for Astrophysics (MPA), New Mexico State University, Ohio State University, University of Pittsburgh, University of Portsmouth, Princeton University, the United States Naval Observatory, and the University of Washington.

Facilities: Sloan

REFERENCES

- Abazajian, K. N., et al. 2009, *ApJS*, 182, 543
 Adelberger, K. L., Shapley, A. E., Steidel, C. C., Pettini, M., Erb, D. K., & Reddy, N. A. 2005, *ApJ*, 629, 636
 Barlow, T. A., & Tytler, D. 1998, *AJ*, 115, 1725
 Becker, G. D., Rauch, M., & Sargent, W. L. W. 2009, *ApJ*, 698, 1010
 Boksenberg, A., Sargent, W. L. W., & Rauch, M. 2003, *ArXiv Astrophysics e-prints*
 Bordoloi, R., et al. 2011, *ApJ*, 743, 10
 Bouwens, R. J., Illingworth, G. D., Franx, M., & Ford, H. 2007, *ApJ*, 670, 928
 Bouwens, R. J., et al. 2010, *ApJ*, 725, 1587
 Chen, H.-W., Lanzetta, K. M., & Webb, J. K. 2001, *ApJ*, 556, 158
 Cherinka, B., & Schulte-Ladbeck, R. E. 2011, *AJ*, 142, 122
 Connolly, A. J., & Szalay, A. S. 1999, *AJ*, 117, 2052
 Cooksey, K. L., Thom, C., Prochaska, J. X., & Chen, H. 2010, *ApJ*, 708, 868
 Danforth, C. W., & Shull, J. M. 2008, *ApJ*, 679, 194
 D’Odorico, V., Calura, F., Cristiani, S., & Viel, M. 2010, *MNRAS*, 401, 2715
 Ellison, S. L., Songaila, A., Schaye, J., & Pettini, M. 2000, *AJ*, 120, 1175
 Faucher-Giguère, C., Lidz, A., Zaldarriaga, M., & Hernquist, L. 2009, *ApJ*, 703, 1416
 Fox, A. J., Savage, B. D., & Wakker, B. P. 2005, *AJ*, 130, 2418
 Frank, S., Mathur, S., Pieri, M. M., & York, D. G. 2010, *ApJ*, 716, 835
 Gauthier, J.-R., Chen, H.-W., & Tinker, J. L. 2010, *ApJ*, 716, 1263
 Haardt, F., & Madau, P. 2001, in *Clusters of Galaxies and the High Redshift Universe Observed in X-rays*, ed. D. M. Neumann & J. T. V. Tran
 Hewett, P. C., & Wild, V. 2010, *MNRAS*, 405, 2302
 Kacprzak, G. G., Churchill, C. W., Barton, E. J., & Cooke, J. 2011, *ApJ*, 733, 105
 Komatsu, E., et al. 2009, *ApJS*, 180, 330
 Lanzetta, K. M., McMahon, R. G., Wolfe, A. M., Turnshek, D. A., Hazard, C., & Lu, L. 1991, *ApJS*, 77, 1
 Martin, C. L., Scannapieco, E., Ellison, S. L., Hennawi, J. F., Djorgovski, S. G., & Fournier, A. P. 2010, *ApJ*, 721, 174
 Matejek, M. S., & Simcoe, R. A. 2012, *ApJ*, 761, 112
 Ménard, B., Wild, V., Nestor, D., Quider, A., Zibetti, S., Rao, S., & Turnshek, D. 2011, *MNRAS*, 417, 801
 Nestor, D. B., Turnshek, D. A., & Rao, S. M. 2005, *ApJ*, 628, 637
 Oesch, P. A., et al. 2010, *ApJ*, 725, L150
 Oppenheimer, B. D., & Davé, R. 2008, *MNRAS*, 387, 577
 Pieri, M. M., Frank, S., Mathur, S., Weinberg, D. H., York, D. G., & Oppenheimer, B. D. 2010a, *ApJ*, 716, 1084
 Pieri, M. M., Frank, S., Weinberg, D. H., Mathur, S., & York, D. G. 2010b, *ApJ*, 724, L69
 Prochaska, J. X., Herbert-Fort, S., & Wolfe, A. M. 2005, *ApJ*, 635, 123
 Prochaska, J. X., O’Meara, J. M., & Worseck, G. 2010, *ApJ*, 718, 392
 Prochaska, J. X., Weiner, B., Chen, H.-W., Cooksey, K. L., & Mulchaey, J. S. 2011, *ApJS*, 193, 28
 Prochter, G. E., Prochaska, J. X., & Burles, S. M. 2006, *ApJ*, 639, 766
 Reddy, N. A., & Steidel, C. C. 2009, *ApJ*, 692, 778
 Richards, G. T., et al. 2002, *AJ*, 123, 2945
 Rubin, K. H. R., Weiner, B. J., Koo, D. C., Martin, C. L., Prochaska, J. X., Coil, A. L., & Newman, J. A. 2010, *ApJ*, 719, 1503
 Ryan-Weber, E. V., Pettini, M., & Madau, P. 2006, *MNRAS*, 371, L78
 Ryan-Weber, E. V., Pettini, M., Madau, P., & Zych, B. J. 2009, *MNRAS*, 395, 1476
 Savage, B. D., & Sembach, K. R. 1991, *ApJ*, 379, 245
 Scannapieco, E., Pichon, C., Aracil, B., Petitjean, P., Thacker, R. J., Pogosyan, D., Bergeron, J., & Couchman, H. M. P. 2006, *MNRAS*, 365, 615
 Schaye, J., Aguirre, A., Kim, T.-S., Theuns, T., Rauch, M., & Sargent, W. L. W. 2003, *ApJ*, 596, 768
 Schaye, J., Carswell, R. F., & Kim, T.-S. 2007, *MNRAS*, 379, 1169
 Schneider, D. P., et al. 2010, *AJ*, 139, 2360
 Shen, Y., et al. 2011, *ApJS*, 194, 45
 Simcoe, R. A. 2006, *ApJ*, 653, 977
 —. 2011, *ApJ*, 738, 159
 Simcoe, R. A., et al. 2010, in *Society of Photo-Optical Instrumentation Engineers (SPIE) Conference Series*, Vol. 7735, Society of Photo-Optical Instrumentation Engineers (SPIE) Conference Series
 Simcoe, R. A., et al. 2011, *ApJ*, 743, 21
 Songaila, A. 2001, *ApJ*, 561, L153
 —. 2005, *AJ*, 130, 1996
 Steidel, C. C. 1990, *ApJS*, 72, 1
 Steidel, C. C., Erb, D. K., Shapley, A. E., Pettini, M., Reddy, N., Bogosavljević, M., Rudie, G. C., & Rakic, O. 2010, *ApJ*, 717, 289
 Weiner, B. J., et al. 2009, *ApJ*, 692, 187
 Wild, V., Hewett, P. C., & Pettini, M. 2006, *MNRAS*, 367, 211
 Wilson, E. B. 1927, *JASA*, 22, 209
 Worseck, G., & Prochaska, J. X. 2011, *ApJ*, 728, 23
 Yip, C. W., et al. 2004, *AJ*, 128, 2603
 York, D. G., et al. 2000, *AJ*, 120, 1579